https://dx.doi.org/10.1016/j.enggeo.2020.105871

DEM modeling of large-scale triaxial test of rock clasts considering realistic particle shapes and flexible membrane boundary

Junqi Zhang
School of Civil Engineering, Central South University, 22 S. Shaoshan Rd., Changsha, Hunan, China
Email: zjq1990@csu.edu.cn

Corresponding author: Xiang Wang*
Department of Civil and Environmental Engineering, The Hong Kong Polytechnic University, Hung Hom, Kowloon, Hong Kong, China.
Email: xiang.wang@connect.polyu.hk

Zhen-Yu Yin
Department of Civil and Environmental Engineering, The Hong Kong Polytechnic University, Hung Hom, Kowloon, Hong Kong, China.
Email: zhenyu.yin@polyu.edu.hk; zhenyu.yin@gmail.com

Zhenyu Liang
School of Civil Engineering, Central South University, 22 S. Shaoshan Rd., Changsha, Hunan, China
Email: liangzhengyu@csu.edu.cn

Abstract: This paper presents a novel framework for the discrete modeling of the large-scale triaxial test of rock clasts, considering both the realistic particle shapes and veritable flexible boundary condition. First, real-shaped particle models for the tested rock clasts are precisely reconstructed using the close-range photogrammetry technique. The rubber membrane was modeled by a series of bonded particles. Then, the laboratory procedures of the triaxial test, i.e., sample preparation, isotropic compression, and shearing, are reproduced in the DEM simulations with consideration of the veritable confining boundary. To ensure more reliable numerical results, a systematic DEM calibration framework is established to determine the modeling parameters based on a series of calibration experiments, including tensile test, suspension test, clast-membrane sliding test, and large-scale triaxial test. Finally, the proposed method is applied to investigate the effects of confining pressure on the macro- and micro-mechanical behaviors of rock clasts. The presented works lay a foundation for further studies on revealing the mechanisms of the conventional triaxial test, e.g., the effect of end restraint and rubber membrane. Moreover, the proposed systematic framework for calibration of modeling parameters can be applied to precisely capture the real mechanical properties of various types of granular rock-like materials in DEM simulations.

Keywords: Rock clast; particle shape; flexible membrane; triaxial test; discrete element method; micromechanics

1 Introduction

Rock clasts, as the most common natural and artificial geomaterials in the world, e.g., gravel, ballast, and other geosynthetic clasts, are widely used in many infrastructure construction projects. The engineering behaviors of rock clasts, which determine the stability and safety of engineering structures during construction and operation, are of great interest to practitioners, designers, and researchers in different fields, e.g., geotechnical engineering, geological engineering, railway engineering, etc. Many engineers and researchers have employed various types of laboratory experiments, e.g., triaxial test (Hu et al. 2018; Indraratna et al. 2013), direct shear test (Han et al. 2018), point load test (Koohmishi and Palassi 2016), repose angle test (Rajan and Singh 2017), etc., to investigate the mechanical properties of rock clasts from different aspects. Among these experiments, the triaxial test is one of the most popular apparatus to study the macroscopic properties, e.g., shear strength parameters, contraction or dilation. Besides, more advanced techniques of the triaxial test have been developed to precisely capture the mechanical features of the materials during testing, including measurement of circumferential displacement (Suiker Akke et al. 2005), dissipation of energy (Li et al. 2017), and movement track of particle (Li et al. 2020) in specimens.

Although many improvements have been implemented, the laboratory triaxial test still has some disadvantages. For instance, the accuracy of data from the test highly depends on the triaxial apparatus and proficiency of operators. The cost of laboratory triaxial test is high, especially for large scale one. The limitation of the apparatus and specimen dimensions results in the restriction that all tested materials should have a maximum particle size smaller than a threshold value due to the well-acknowledged size effect mechanism (Indraratna et al. 2011; Yin et al. 2017). Additionally, the initial fabric of the sample, which is difficult to be controlled and observed in laboratory experiments, greatly affects the test results (Chang and Yin 2010; Yang and Dai 2011; Yin et al. 2010). Besides, the effects of the rubber membrane and end restraint from the triaxial apparatus still remains unclear and cannot be ignored in large shear strain (Cheung and O'Sullivan 2008; Muraro and Jommi 2019). Therefore, behaviors of granular materials at the critical state cannot be precisely captured through triaxial testing. In consequence, numerical methods (DEM, FEM, and FDM) are developed to perform virtual triaxial tests. Among them, the discrete element method has shown a great capability to investigate the micromechanical particle mechanics with physics insight (Goldenberg and Goldhirsch 2005; Wang and Yin 2020), e.g., the particle movement, coordination number, fabric anisotropy, contact force network, sliding contact percentage, and inter-particle normal and shear contact forces.

In the discrete element method (DEM), cubic compression with rigid boundary condition was first proposed to mimic the similar stress state during the triaxial test (Cheng et al. 2003). Then, considering the shape of specimens in real laboratory triaxial tests, rigid cylindrical sidewalls were adopted (Gao and Meguid 2018) with a collaborative servo-control mechanism. To consider the end restraint effect of the triaxial test, layered cylindrical walls were used to simulate the boundary (Liu et al. 2019). In order to reproduce the failure mode of specimens in the triaxial test, equivalent force algorithms were suggested to replace the servo mechanism of sidewalls to apply confining pressure (O'Sullivan and Cui 2009). Recently, a new servo mechanism, which used bonded particles to simulate the rubber membrane, was proposed to model the confining boundary of specimens in the triaxial test (Li et al. 2017; Qu et al. 2019). Nevertheless, in the previous investigations, the bending resistance of the rubber membrane in the bond-particle algorithm was ignored, which was recently solved by FDM-DEM coupling method (Zhu and Yin 2019; Zhu et al. 2020). However, the particle shape, known as a key factor affecting the shear behaviors (Yin et al. 2020), was not involved. Moreover, numerical studies of the large-scale triaxial tests considering both the rubber membrane boundary and real rock clast shapes have not been reported.

To fill the research gaps, we propose a numerical framework for DEM modeling of large-scale triaxial tests with a systematic calibration process considering the particle shape and confining boundary. First, realistic particle models for the tested rock clasts are precisely restructured based on the close-range photogrammetry technique. Then, the realistic confining boundary is reproduced using the cluster-based membrane model. The process of the numerical triaxial test is then illustrated according to the laboratory test processes. In addition, a systematic procedure for determining the modeling parameters is given based on a series of calibration experiments. Finally, the proposed method is applied to investigate the behaviors of the tested rock clasts with different confining pressures from both micro and macro perspectives.

2 Veritable reconstruction and shape analysis of rock clasts

2.1 Sampling of rock clasts

The source material of the selected rock clasts is the crushed granite obtained from Changsha (Hunan Province, China), which is also the source of the ballast layer in the Liuyang section of the Menghua heavy haul railway. In the preparation of the experiment, rock clasts with crushable shape (easy to break, e.g., high elongation and flatness (Ministry 2008)) are manually eliminated from the source materials, as shown in Fig. 1.

Fig. 1 Selection of the rock clasts

According to the American Railway Engineering and Maintenance-of-Way Association (AREMA) No. 3 gradation, the adopted particle size distribution (PSD) of the rock clasts is shown in Fig. 2. Moreover, the density of the clast ρ_c is 2710 kg/m^3, and the maximum dry density and optimum moisture content of specimens are 1.81g/cm^3 and 0.5%, respectively, following the ASTM D1557 (ASTM 2012).

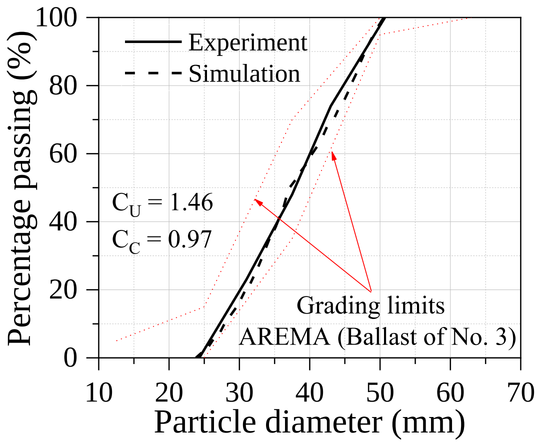

Fig. 2 Particle size distribution of the clasts.

2.2 Photogrammetry-based reconstruction of rock clasts

Particle shape is a key factor to affect the interlocking in the granular medium (Suhr et al. 2020), and highly correlated with the strength of rock clasts (Koohmishi et al. 2016). Close-range photogrammetry, a photo-based technology in 3D reconstruction, is used to acquire shape features of clasts in this study. This technology has been applied in many fields, such as architectural design, industrial processing, civil engineering, and biomedical fields. According to the existing literature (Paixão et al. 2018), compared with other technologies (laser scanning, CT scanning, etc.), close-range photogrammetry can more quickly obtain the surface topography information (including color information and geometric information) of the target object. In addition, the technology has high accuracy, low cost, and does not cause damage to the target object. In order to obtain the shape features, three industrial cameras, a rotary turntable, and a photo studio with astral lamps are established to acquire multiple images surrounding the particle surface. The 3D reconstruction scheme is shown in Fig. 3 (*a*). Rotating the turntable (5° per second) and taking continuous photos of the clast (6 seconds per shot), three industrial cameras shot from the three elevation angle directions (15°, 45° and 75°). Since the shape information of the clast base could not be collected, overturn the clast and repeat the same shooting process. Finally, a total of 60 photos can be obtained for each clast.

The commercial software Photoscan (Li et al. 2016) is employed to process the clast photos and reconstruct the 3D particle model. First, feature points are extracted and registered from the photos, and then the feature points of the clast are reconstructed sparsely using the motion restoration structure method to construct a sparse point cloud. The sparse points in the point cloud are used as seed points to determine more points based on block matching. Next, the Poisson reconstruction is performed on the reconstructed 3D point cloud to build the triangular meshes of the particle surface. Finally, the triangular meshes model is output as STL file for simulation usage. In this study, a total of 100 rock clasts are randomly selected for 3D reconstruction, and some example clasts are shown in Fig. 3 (*b*).

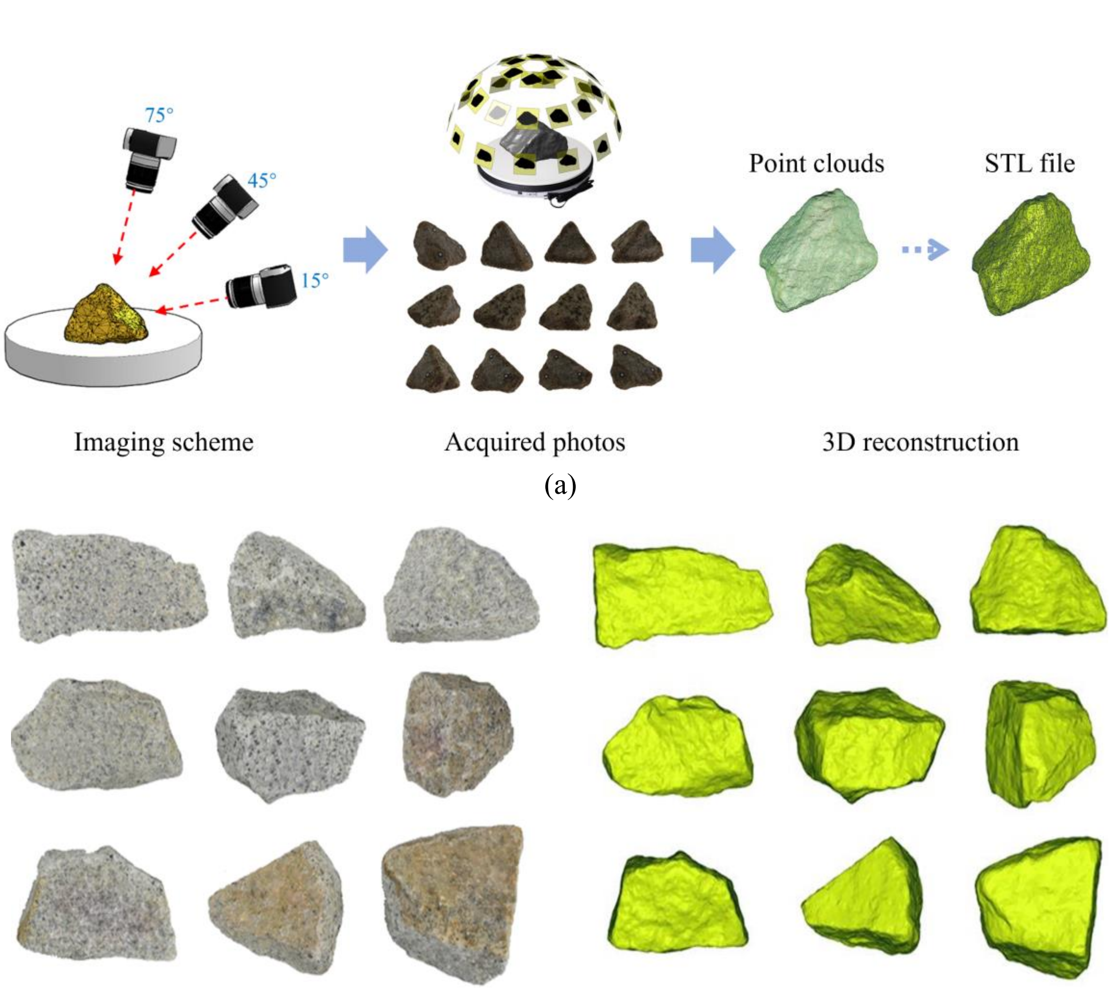

Fig. 3 Digital image acquisition platform: (a) 3D reconstruction and (b) examples of reconstructed rock clasts

2.3 Particle shape quantification of rock clasts

Four typical shape indexes from three levels are adopted to quantify the shape features of rock clasts. The four shape indexes, e.g., elongation index (EI), flatness index (FI), roundness (Rd), and roughness (Rg), were often used for particle shape evaluation in previous researches (Barrett 1980; Wang 2020).

The elongation index EI and flatness index FI reflect the flake degree and acicular degree, respectively, and the larger the value, the closer the particle tends to the cube or sphere. The EI and FI are calculated based on the dimension of curcumscribed oriented bounding box of the rock clast, which can be determined based on the 3D Minkowski tensor Ω_{ij}:

$$\Omega_{\mathrm{ij}} = \frac{1}{S_M}\sum_{k=1}^{N_m} s^k T_i^k T_j^k \tag{1}$$

where T_i^k and T_j^k are the i^{th} and j^{th} components of the unit normal vector of k^{th} triangular mesh, shown in Fig. 4 (*a*). s^k is the area of k^{th} triangular mesh. N_m and S_M are the number and the total area of triangular meshes, respectively. Ω_{ij} is corresponding to the symmetric matrix C with trace 1:

$$C = \begin{bmatrix} \Omega_{11} & \Omega_{12} & \Omega_{13} \\ \Omega_{21} & \Omega_{22} & \Omega_{23} \\ \Omega_{31} & \Omega_{32} & \Omega_{33} \end{bmatrix} = [q_a \quad q_b \quad q_c] \begin{bmatrix} \lambda_a & 0 & 0 \\ 0 & \lambda_b & 0 \\ 0 & 0 & \lambda_c \end{bmatrix} \begin{bmatrix} {q_a}^T \\ {q_b}^T \\ {q_c}^T \end{bmatrix} \tag{2}$$

where the three eigenvalues $(\lambda_a \geq \lambda_b \geq \lambda_c)$ are the minimum proportions of the projected area of the particle in the corresponding principal axis direction to the total area. q_a, q_b and q_c are three principal axis directions of the oriented bounding box (OBB).

After determining the three principal directions of the particle, the OBB of the particle can be constructed along the principal direction, as shown in Fig. 4 (*a*). Then, EI and FI can be expressed as:

$$EI = \frac{I}{L} \tag{3}$$

$$FI = \frac{S}{I} \tag{4}$$

where L, I and S are the largest, intermediate, and smallest length in the direction of the principal axis of the OBB, respectively.

The particle roundness Rd is a well-known shape index proposed by Wadell (Wadell 1932) to evaluate the relative sharpness of particle corners. Based on the algorithm of the largest inscribed sphere and the local inscribed sphere of the corner (Itasca 2014), the three-dimensional roundness Rd is calculated as follow:

$$Rd = \frac{1}{N_C}\sum_{i=1}^{N_C} r_i \Big/ R_{insc} \tag{5}$$

where R_{insc} indicates the radius of the largest inscribed sphere. r_i is the radius of i^{th} inscribed sphere of the local corner and N_C is the number of the identified corners.

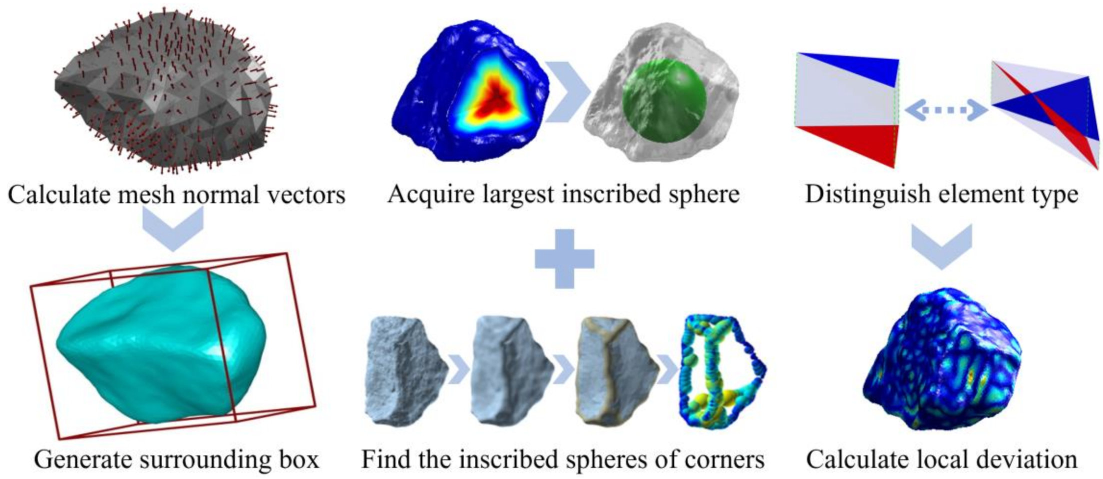

(a) (b) (c)

Fig. 4 Calculation processes of shape indexes: (a) elongation index (EI) and flatness index (FI), (b) roundness (Rd) and (c) roughness (Rg)

The process of calculating Rd is demonstrated in Fig. 4 (b). In order to find the largest inscribed sphere, the rock clast is voxelized according to the STL file. Then, go through all the voxelized spaces and sum up the distance from the center of space to the surface of clast. The center of space, corresponding to the minimum sum, is the center of the largest inscribed sphere. Moreover, the method to acquire the local inscribed corner spheres includes three major steps, e.g., surface smoothing, corner identification, and sphere fitting, which are detailed in (Wang 2020).

As shown in Fig. 4 (c), the roughness (Rg), as a shape index in the third level, is calculated based on the author's previous study. It is conducted through (1) fitting the points cloud of the clast surface by the high-order spherical harmonics; (2) established benchmark smoothed surface with lower-order spherical harmonics; (3) compare the original and benchmark surface and calculate the local deviation distance Δd_i. The deviation distance equals to the volume of deviation area divided by the area of the local triangular element. The definition of the roughness Rg is given as:

$$Rg = \sqrt[3]{\frac{4\pi}{3V_a}} \cdot \frac{1}{S_M} \sum_{i=1}^{N_m} \Delta d_i \times S_i \tag{6}$$

where S_i is the area of i^{th} triangular mesh element; V_a is the volume of the clast; N_m is the number of triangular mesh element; S_M is the area of the clast surface.

As shown in Fig. 5, the shape results of 100 randomly selected rock clasts are statistically presented. Because of manually selection to eliminate the undesired shapes, both EI and FI have similar distributions and range from 0.5 to 1.0, as shown in Fig. 5 (*a*) and (*b*). It means that the clasts are mostly massive, with few flakes and needles. The results roundness index Rd are shown in Fig. 5 (*c*). It can be seen from the figure that over 98% of the tested rock clasts had an Rd greater than 0.2 and all the Rd is smaller than 0.4. Moreover, as shown in Fig. 5 (*d*), the roughness of the clasts Rg is in the range of [0.05, 0.14] and Rg around 0.08 is obviously redundant with other intervals.

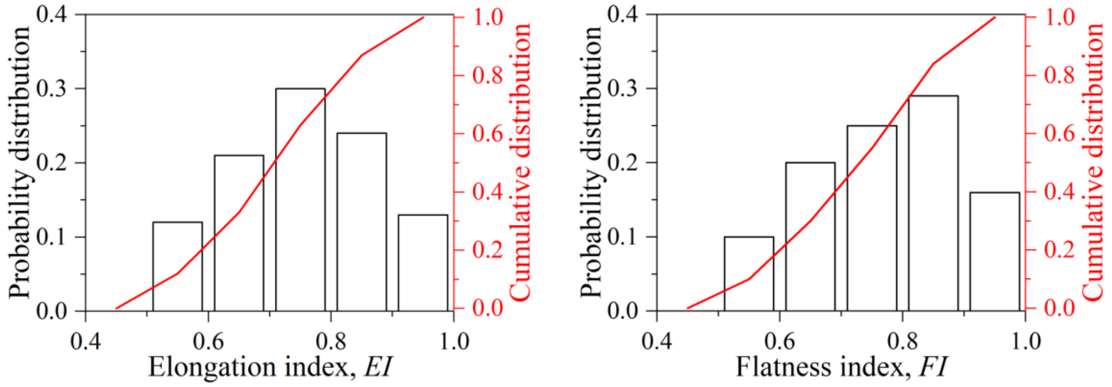

(a) (b)

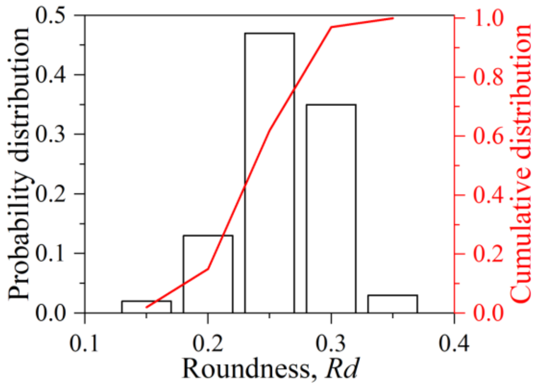

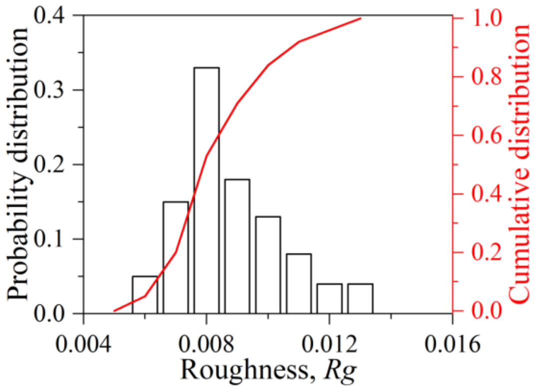

(c) (d)

Fig. 5 Statistics of shape indexes: (a) elongation index ($\boldsymbol{EI}$), (b) flatness index ($\boldsymbol{FI}$), (c) roundness ($\boldsymbol{Rd}$) and (d) roughness ($\boldsymbol{Rg}$)

3 Modeling of the large-scale triaxial test

The DEM software PFC^{3D} 5.0 has been proved to be a reliable numerical tool for investigating the granular materials with realistic shape from the microscale perspective (Liu et al. 2017). This study adopts the code PFC^{3D} 5.0. Numerical triaxial tests of rock clasts are performed considering realistic particle shapes and veritable membrane boundary.

3.1 DEM model of rock clast with realistic shapes

In this study, the clump-based particle model (rigid agglomerate), which approximates the rock clast shape with an agglomerate of rigid spheres according to Itasca (Itasca 2014), is employed to model the realistic-shaped rock clasts. The clump-based particle models in DEM are created using the triangular-mesh-based particle models obtained from the above-described photogrammetry-based 3D scanning. As shown in Fig. 6 (*a*), there are two key parameters, e.g., 'Distance' and 'Ratio', that control the shape of the generated clump-based particle model. The 'Distance' corresponds to an angular measure of smoothness in degrees from 0 to 180, and the 'Ratio' is the radius ratio of smallest pebble to largest pebble in the clump template. As shown in Fig. 6 (*b*), the 'Distance' and the 'Ratio' strongly affect the roughness of the model surface and the sharpness of edges and corners. In this study, in order to determine the appropriate values of 'Distance' and 'Ratio', the two parameters are varied within certain ranges, e.g., 80 ≤ 'Distance'≤ 160, and 0.1 ≤ 'Ratio'≤ 0.5, which cover most of the adopted values in the previous studies of realistic clast modeling (Liu et al. 2017; Miao et al. 2017).

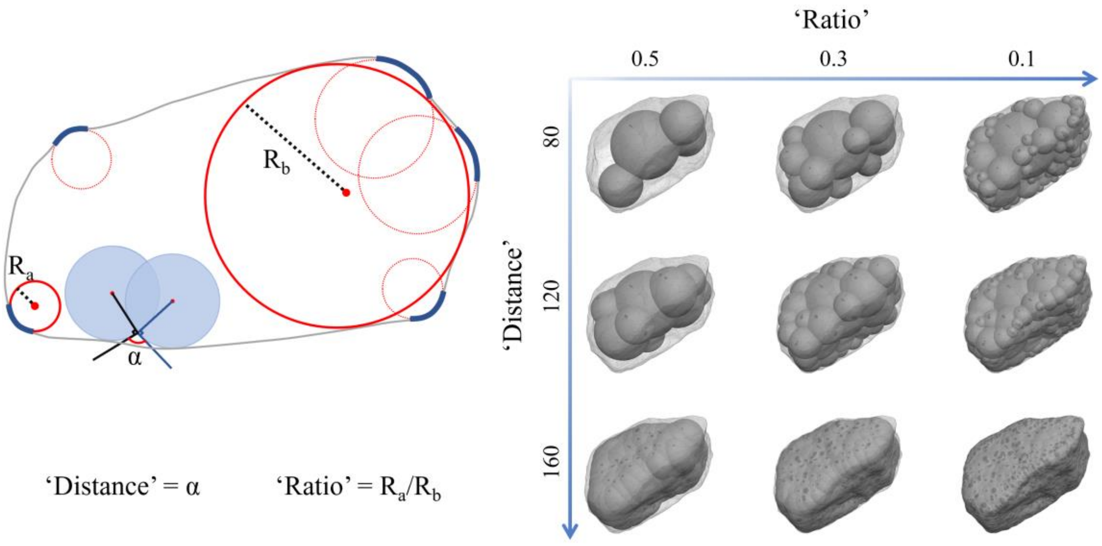

(a) (b)

Fig. 6 key indexes in the generation of clump templates (a) meaning and (b) influence

The adoption of 'Distance' and 'Ratio' in DEM simulation should consider the balance of both computation efficiency and simulation accuracy. Thus, the average pebble amount in clump template N_p and the filling rate of clump template R_f, which are affected by both 'Distance' and 'Ratio', are compared in the chosen area. The filling rate of the clump template R_f is defined as:

$$R_f = \sum_{i=1}^{N_t} \frac{DT_i}{DS_i} \times 100\% \tag{7}$$

where N_t is the number of STL file and equals to 100 in this study. DT_i is equivalent diameter of clump template generated by i^{th} STL file, and DS_i is the equivalent diameter of i^{th} STL file. The equivalent diameter of the rock clast is the diameter of a sphere which has the same volume with the clast.

Fig. 7 displays the variation of R_f (values in z-axis coordinates) and N_p (values in blue numbers) with different 'Distance' (80°, 100°, 120°, 140°, 160°) and 'Ratio' (0.1, 0.2, 0.3, 0.4, 0.5). D140-R04 (the abbreviation of the template with 'Distance'=140 and 'Ratio'=0.4), D120-R03 and D100-R02 are chosen as candidates because of the balance between R_f and the gradient of N_p. As shown in the example template in Fig. 7, the surface of D140-R04 is more realistic than that of D100-R02, while the angularity of D100-R02 is more accurate. Since the influence of an unreal surface will be compensated by the assigned friction coefficient of the clump-based particle model, the 'Distance' and 'Ratio' is adopted as 100 and 0.2, respectively. Accordingly, the average pebble amount in clump template N_p is 59.7 which is larger than the most of previous numerical simulations (Gao and Meguid 2018; Lu and McDowell 2006; Tong and Wang 2014).

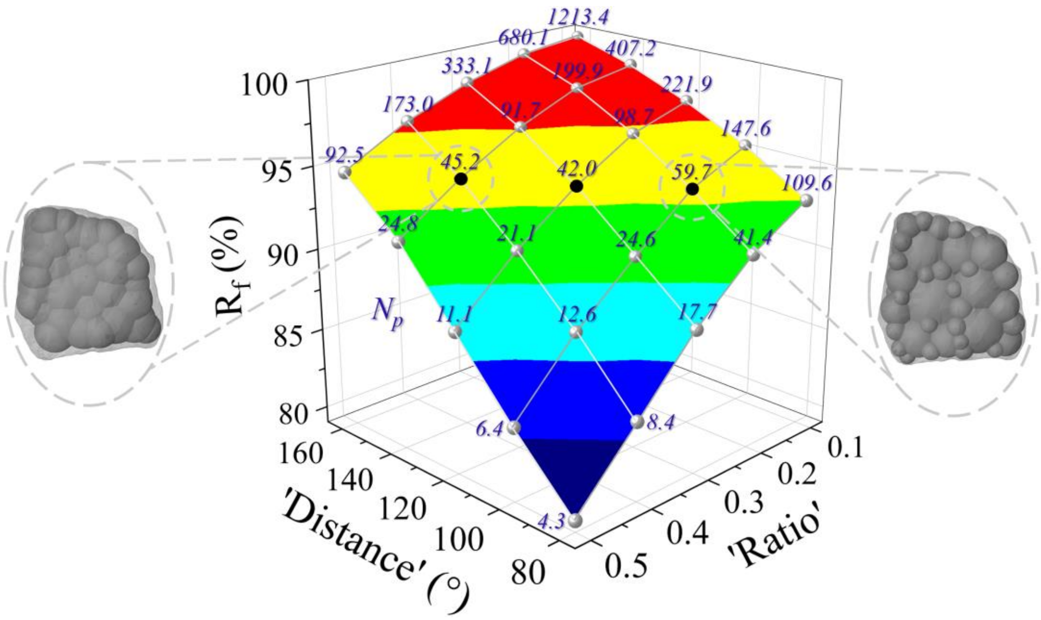

Fig. 7 Variation of R_f and N_p with different 'Distance' and 'Ratio'

3.2 Adopted contact models in the DEM simulation

Two contact models are involved in the simulation of the triaxial compression test of rock clasts, including the linear elastic model and the simplified linear parallel bond model. As shown in Fig. 8 (*a*), the linear elastic contact model (Gong et al. 2019b) is adopted to simulate the interactions between different objects, including clast-clast contact, clast-membrane contact, clast-wall contact, membrane-membrane contact, and membrane-wall contact. The wall is employed to simulate the top and base steel plate. In the linear elastic model, the contacts cannot resist the bending moment and tensile force and will ultimately undergo linear elastic deformation and slide under compression. The force-displacement relationship can be expressed as:

$$F_n = k_n u_n \tag{8}$$

$$F_t = \begin{cases} k_t u_t & k_t u_t < \mu F_n \\ \mu F_n & k_t u_t \geq \mu F_n \end{cases} \tag{9}$$

where F, u and k are the contact force, contact displacement, and linear contact stiffness, respectively. The subscript n and t indicate the normal direction and tangential direction. μ is the friction coefficient. Considering that the contact stiffness is closely related to the shape of the contact point, effective modulus E and stiffness ratio kr are used to describe the different contact stiffness in, which defined as:

$$E = \begin{cases} \dfrac{k_n(r + r')}{\pi(\min(r, r'))^2)} & \text{Particle-Particle contact} \\ \dfrac{k_n}{\pi r} & \text{Particle-Wall contact} \end{cases} \tag{10}$$

$$kr = \frac{k_n}{k_t} \tag{11}$$

where r and r' are the radius of the first particle (particle is a basic element in PFC^{3D} 5.0 and also named ball) and second particle, respectively. Eq. (10) indicates that the deformation (overlap) of particle-wall contact completely depends on the stiffness of particle in PFC^{3D}, and the wall is always regarded as ‘rigid’.

Deformable agglomerates (clusters) are employed to simulate the rubber membrane, in which a certain number of particles with the same sizes are bonded together using a simplified linear parallel bond model. The typical linear parallel bond model includes a bond component and a linear component, and the two components act in parallel. According to the assumption that rubber shows similar elastic behavior in both tension and compression under certain strain (Asadi et al. 2018a), the linear parallel bond model is simplified that the stiffness of the linear component is set to zero. In other words, the linear component is deleted, and the retained bond component provided linear elastic behavior. Moreover, the strength of the bond model is large enough to prevent the membrane from breakage during the triaxial test. The simplified linear parallel bond model is shown in Fig. 8 (*b*). The force-displacement relationship can be expressed as:

$$F_n = \bar{A}\bar{k}_n u_n \tag{12}$$

$$F_t = \bar{A}\bar{k}_t u_t \tag{13}$$

where $\bar{k}_n$ and $\bar{k}_t$ are the parallel bond normal stiffness and the parallel bond tangential stiffness, respectively. $\bar{A}$ is the contact area between bonded particles and equals to $\pi\bar{R}^2$ ($\bar{R}$ is half of the membrane thickness in this study). Moreover, the bending moment M_b and the twisting moment M_t are defined as:

$$M_b = 0.25\pi\bar{R}^4\bar{k}_n\theta_b \tag{14}$$

$$M_t = 0.5\pi\bar{R}^4\bar{k}_t\theta_t \tag{15}$$

where θ_b and θ_t are bend-rotation and twist-rotation, respectively.

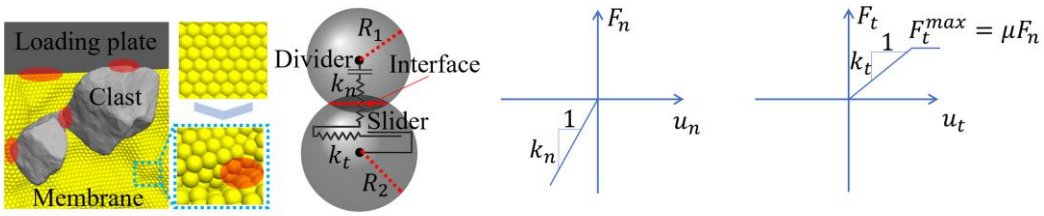

(*a*)

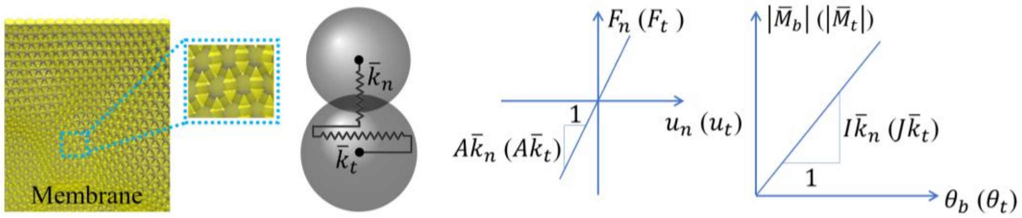

(*b*)

Fig. 8 Adopted contact models: (*a*) linear elastic model and (*b*) simplified linear parallel bond model

3.3 Confining pressure activated by the flexible membrane

Considering the consistency between the numerical simulation and the laboratory test, the cluster-based model of a flexible membrane is established, and the confining pressure is applied to the specimen through the membrane-based servo control process, which is improved from the previous work (Li et al. 2017).

As shown in Fig. 9, the cluster-based membrane model is established by approximating the cylindrical membrane surface using a series of bonded particles in DEM. The detailed process to set up the membrane model is described as follow:

(1) Generate rigid walls according to the realistic shape and size of the specimen in the laboratory test, including top wall (loading plate), base wall (base plate), and sidewalls (cylindrical container).

(2) Determine the distance between the centers of two bonded particles. In order to protect the cluster-based membrane from puncture, bonded particles should have a certain amount of initial overlap. In this study, the distance of centers between two bonded particles is defined as 0.72 times the particle diameter (thickness of membrane).

(3) Partition the cylindrical container surface into triangular meshes. All the triangular meshes are the

same equilateral triangles, and the length of the edge of triangles is equal to the distance between the centers of two bonded particles. Output the node positions of the triangular meshes.

(4) Create the bonded particles, and the particle centers are determined by the obtained node positions. Assign the simplified parallel bond model to the contact between each pair of neighboring bonded particles after the creation process.

(5) Finally, the cylindrical container is replaced by the cluster-based membrane model, which can be employed to activate the confining pressure by applying the external forces to the bonded particles.

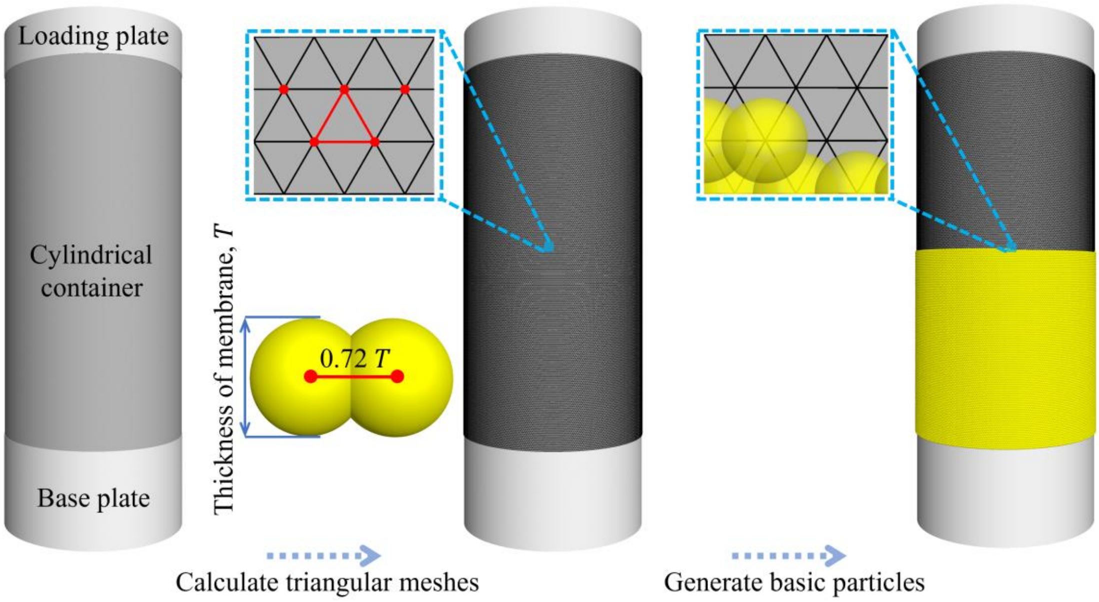

Fig. 9 Generate of bonded particles in the rubber membrane

As described above, the undeformed membrane is approximated by the equilateral triangular elements, in which one particle is bonded with six neighboring particles to form a hexagonal arrangement. The external force is manually applied to each particle element according to the confining pressure and the local distortion of the membrane. Essentially, the magnitude of the applied force on the particle element is the product of the confining pressure and the area of the equivalent region. Moreover, the applied force is perpendicular to the equivalent region and pointed inward to the specimen. As shown in Fig. 10, the equivalent region of the bonded particle 0 (node 0 is the center of particle 0) is affected by surrounding six triangular mesh elements, and the acting force on the triangular mesh element 034, which arises from the confining pressure σ_c, can be express as follow:

$$\vec{f}_{034} = \frac{\sigma_c}{2}\vec{l}_3 \times \vec{l}_4 \tag{16}$$

where $\vec{l}_3$ (or $\vec{l}_4$) is defined as the vector pointing from node 0 to node 3 (or 4).

The acting force $\vec{f}_{034}$ spreads equally to node 0, node 3, and node 4. Moreover, the applied force on node 0 is provided by acting the force on six surrounding triangular mesh elements. Thus, the applied force on node 0 is defined as:

$$\vec{f}_0 = \frac{\sigma_c}{6}\sum_{n=1}^{6}\vec{l}_{n+1} \times \vec{l}_n \tag{17}$$

where $\vec{l}_n$ (or $\vec{l}_n$) is defined as the vector pointing from node 0 to node n (or $n+1$).

For a triangular mesh element m, we can calculate the center coordinate (x_m, y_m, z_m), the outward normal (X_m, Y_m, Z_m), and the area A_m. Thus, according to the divergence theorem of Gauss, the volume of the specimen can be calculated:

$$Vol = \iiint_V dV = \oiint_S X_m \cdot x_m dS \approx \sum_{m\in V} A_m X_m x_m \tag{18}$$

Moreover, to simulate the end restraint of the specimen, the top and base bonded particles (highlighted in red as shown in Fig. 10) are fixed to the contacted walls, i.e., the particle velocity is equal to the wall velocity. It worth noted that when the local distortion of the rubber membrane is large, new contacts between none-neighboring bonded particles will exist. In this case, the linear elastic model is employed as the contact law to simulate the interaction between none-neighboring bonded particles, which are denoted as membrane-membrane contacts, abbreviated as m in subscript. The effective modulus E_m, stiffness ratio kr_m and friction coefficient μ_m are assigned to the membrane-membrane contacts. Besides, considering the initial overlap of bonded particles, the density of bonded particles are assigned as 809 kg/m^3 based on the real density of rubber membrane ρ_m (941 kg/m^3) in this study.

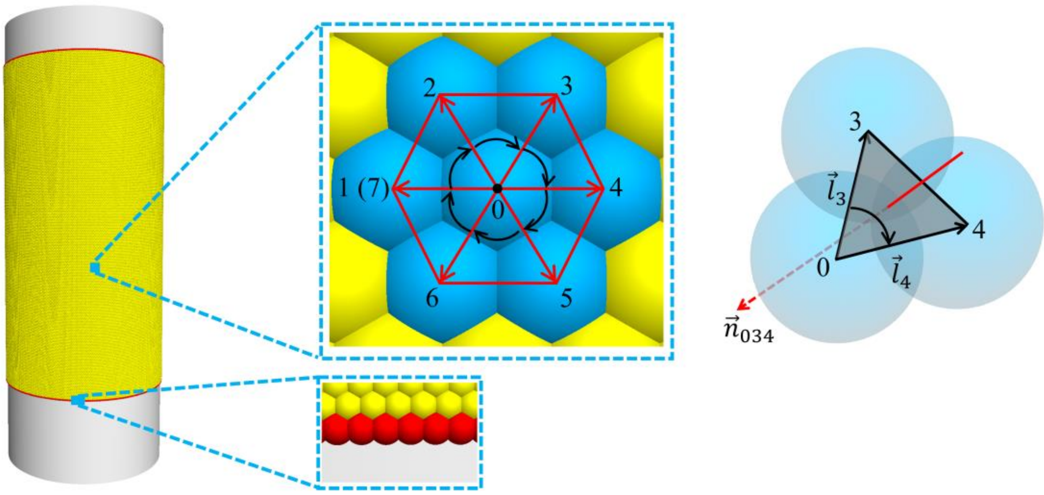

Fig. 10 Calculation of applied force in each particle element

3.4 Simulation process of the triaxial test

In this section, the simulation of the large-scale triaxial test is performed to mimic the real procedures of the laboratory experiment. Considering the working condition of the rock clasts (e.g., ballast), we focus on the consolidated drained monotonic triaxial test. According to ASTM D7181 (ASTM 2011), the laboratory experiments are carried out following three stages, i.e., sample preparation, isotropic compression, and shearing. It worth noted that the dry granular material has same behavior of saturated one, and thus the saturation is not necessary considered in DEM simulation. The adopted conventional large-scale triaxial apparatus is shown in Fig. 11. The bottom of the specimen is fixed on a base steel plate, and the top of the specimen is covered by a steel loading plate, which can move down vertically and freely. The water in the chamber is employed to activate the confining pressure on the rubber membrane around the specimen.

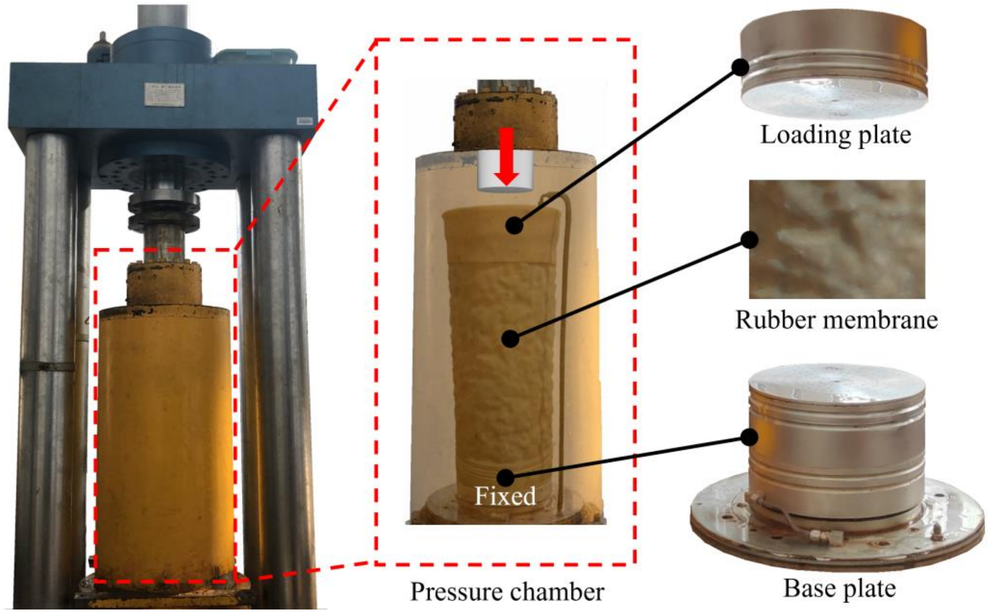

Fig. 11 The large triaxial apparatus in this study

Since the weight of the large triaxial test specimen is very large, and the rubber membrane is delicate, the specimen preparation process is conducted with great carefulness on the triaxial apparatus. The rock clasts are compacted layer by layer for three times in a cylindrical steel container, which is 300 mm in diameter and 600 mm in height. The thickness and designed void ratio of each layer are always kept as 200 mm and 0.56 (equal to 95% compaction degree), respectively. According to the laboratory test, as shown in Fig. 12 (*a*), three layers of rock clasts are generated and compacted successively in DEM simulation. The numerical process is detailed as follow:

(1) Firstly, for each layer, non-overlapping clasts are randomly generated in the rigid cylindrical container. The total volume of generated clasts is in line with the real volume for each layer in the laboratory test. Then, a compaction friction coefficient μ_0 is assigned, and the generated rock clasts fall freely with the same gravitational acceleration (9.7915 m/s^2 in Changsha).

(2) Next, a compaction wall is created at the top of the specimen and move down to apply compaction load to the rock clast until a designed void ratio is reached.

(3) Then, the compaction wall is lift up and the rebound height is computed. If the rebound height

exceeds 1 cm, redo the compaction until the rebound height is smaller than 1 cm.

(4) If the rebound height is still larger than 1 cm after many times of compaction, delete the whole layer of rock clasts and repeat step (1) to step (3) until the rebound height is smaller than 1 cm. It worth noted that when repeat the sample generation and compaction process, a new pseudorandom number would be updated in PFC^{3D} to ensure a different spatial pattern (positions and orientations) of the generated rock clasts and the compaction friction coefficient will be adjusted carefully to reduce the interlocking of clasts during free falling and compaction.

(5) Finally, after a total of three layers of rock aggregated are generated and compacted to reach the target void ratio, as shown in Fig. 12 (*b*), the compaction wall is deleted, and the real friction coefficient is assigned to all the particles.

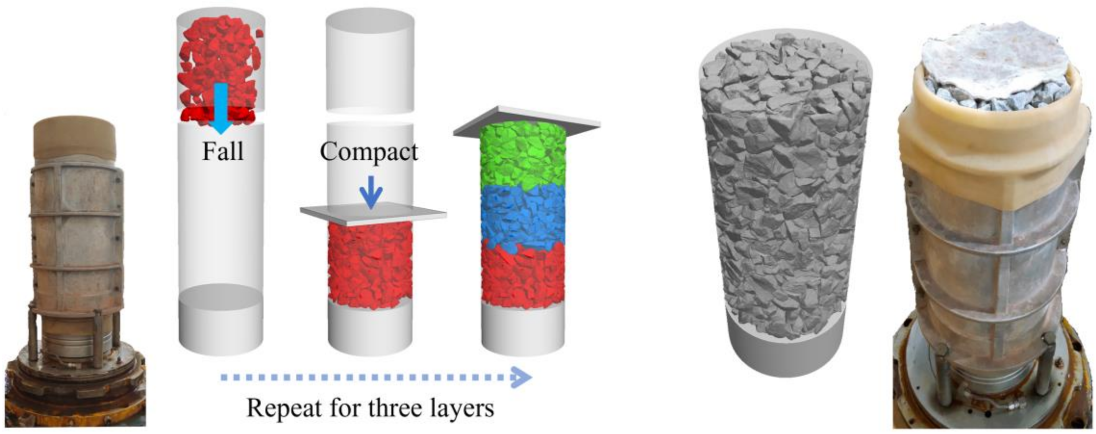

(*a*) (*b*)

Fig. 12 Compaction process: (*a*) compaction in three layers and (*b*) comparison of the compacted specimen between numerical and laboratory test

After the compacted specimen is well prepared in Fig. 13 (*a*), the next process is to activate the confining pressure, named the consolidation process under isotropic compression, which is performed based on the following steps:

(1) First, replace the rigid cylindrical sidewalls with the cluster-based membrane model, as shown in

Fig. 13 (*b*). The thickness of the numerical membrane is equal to the actual rubber membrane in a laboratory test (2.5 mm). Generate a new loading plate on the top of the specimen to mimic the real one shown in Fig. 11.

(2) Then, the lateral confining pressure σ_c is activated based on the previously introduced membrane servo method, in which the specified force is applied to each bonded particle according to Eq. (17). Meanwhile, the bottom wall is fixed, and the axial confining pressure is activated based on the wall-servo control process of the loading plate (top wall). The wall-servo control is a well-acknowledged process, in which a specific wall velocity is updated in real-time according to the contact force and stiffness measured from the loading wall at each time step (Gong and Liu 2017).

(3) The specimen is assumed to reach the consolidated state, as shown in Fig. 13 (*c*), when two numerical conditions are satisfied at the same time: (*a*) the unbalanced ratio, defined as the ratio of the mean unbalanced force to the mean contact force (Farhang and Mirghasemi 2017), is less than 10^{-5}; and (*b*) the deviation between measured confining pressure and the target one is less than 0.1%.

It can be seen from Fig. 13 (*c*) and (*d*) that the consolidated numerical specimen is visually consistent with the experimental one. It worth noted that since the pressure chamber is not transparent, the illustrated experimental consolidated specimen in Fig. 13 (*d*) is made by a vacuum pump, and the pressure difference is approximately equal to the confining pressure.

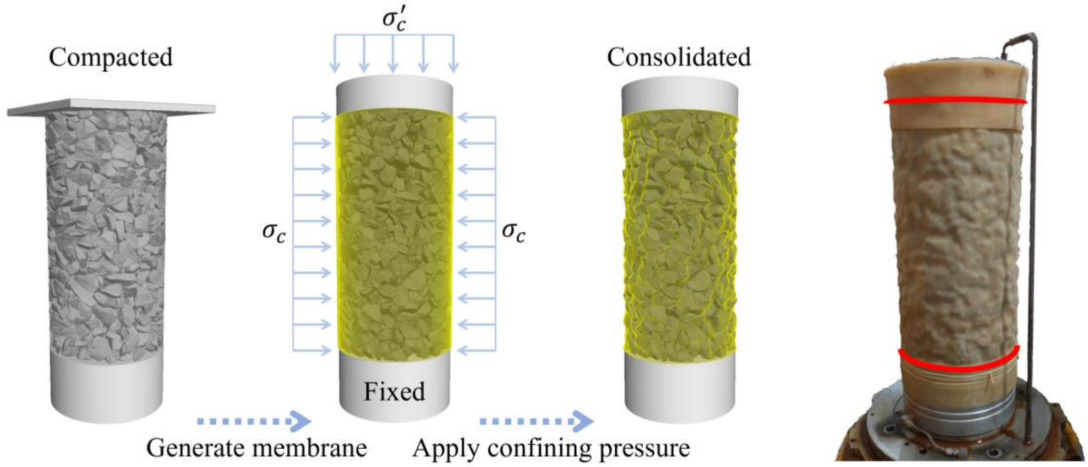

(a) (b) (c) (d)

Fig. 13 Numerical consolidation process: (a) compacted specimen in rigid boundary, (b) replace rigid boundary, (c) consolidated specimen in simulation and (d) consolidated specimen in laboratory test

Once the consolidated specimen is ready, the final step is to activate the axial compression load. As shown in Fig. 14 (*a*), the loading plate is moved down at a constant velocity in the shearing process, while the particle elements of the membrane moved independently to provide constant confining pressure. To obtain a quasi-static behavior, the shear strain rate $\dot{\varepsilon}_1$ (the ratio of loading velocity to specimen height) is sufficiently small according to the inertia number $I_{inertia}$ introduced by MiDi (2004):

$$I_{inertia} = \dot{\varepsilon}_1 \frac{d_c}{\sqrt{\sigma_c/\rho_c}} < 10^{-3} \tag{19}$$

where d_c is the average clast diameter, and ρ_c is the density of clast. In this study, the shear velocity is constant (0.05 times the initial height of the specimen). Thus, $\dot{\varepsilon}_1$ is Approximately equal to 0.05. Accordingly, $I_{inertia}$ is less than 10^{-4} during shear.

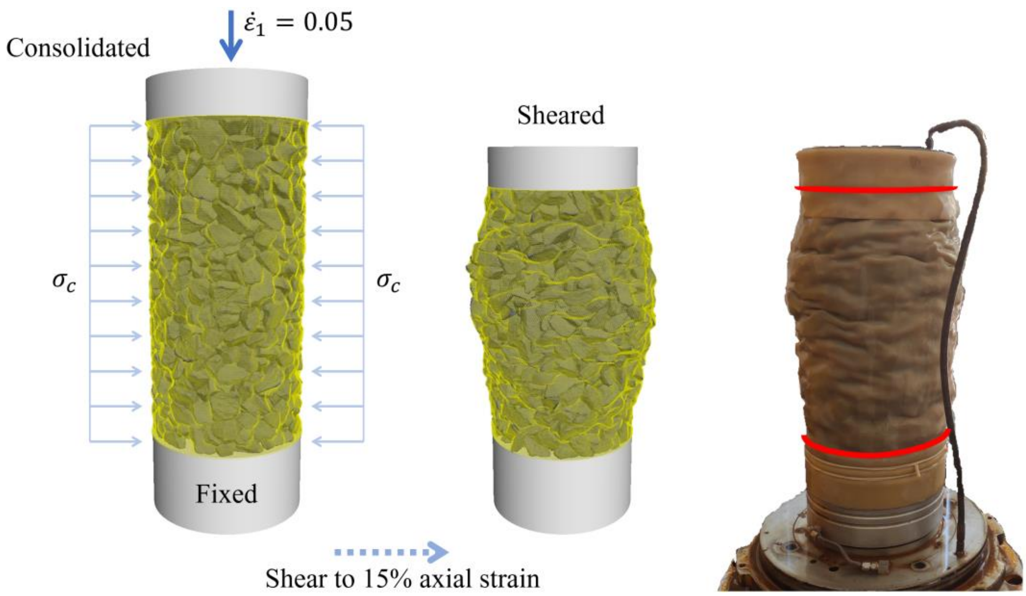

(a) (b) (c)

Fig. 14 Shearing process: (a) packed specimen (b) sheared specimen and (c) sheared specimen in laboratory test

The shearing process continues until the axial strain reached 15%, which is consistent with the laboratory test. As shown in Fig. 14 (*b*) and (*c*), the overall deformation of the numerical specimen at the final shear state is very similar to the realistic one. The simulation process of the large scale triaxial compression test is summarized in Fig. 15.

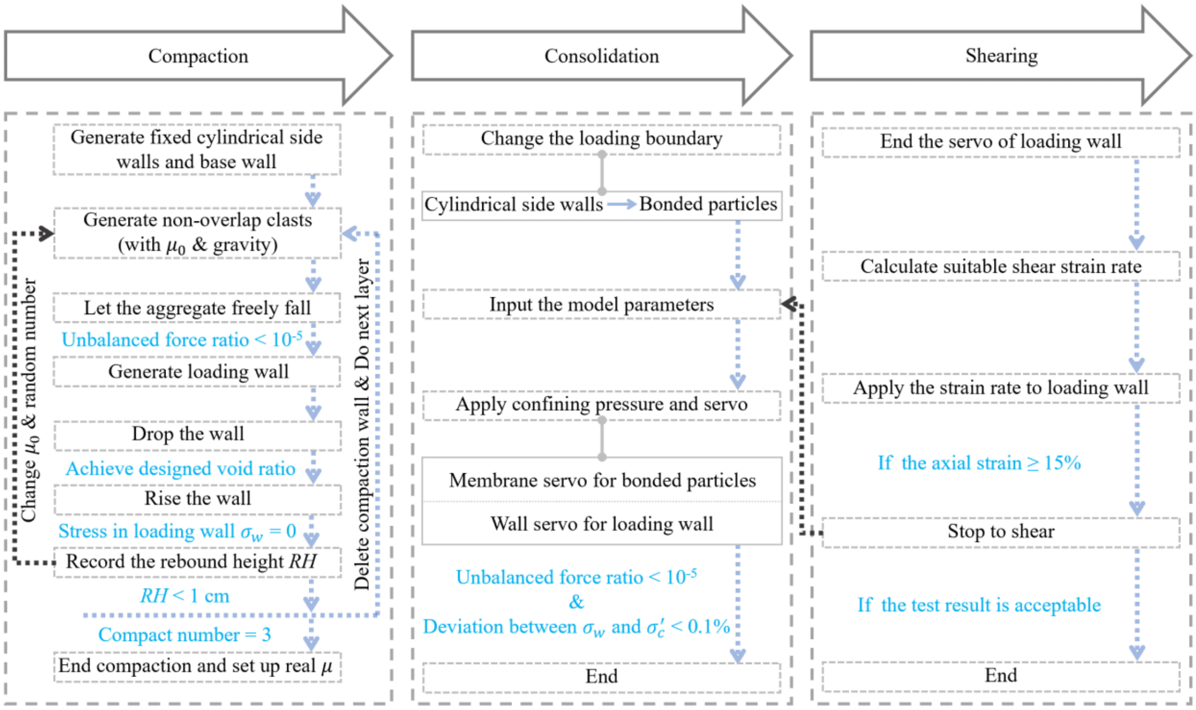

Fig. 15 Process of numerical triaxial compression test

It worth noted that, to be consistent with the laboratory experiment, the axial strain ε_1, volumetric strain ε_v and deviatoric stress q in this study are defined following the ASTM D7181:

$$\varepsilon_1 = \frac{h_0 - h}{h_0} \tag{20}$$

where h_0 and h are the height of specimen in initial and current, respectively.

The volumetric strain ε_v is given as follows:

$$\varepsilon_v = \frac{V_0 - V}{V_0} \tag{21}$$

where V_0 and V are the volume of the specimen in the initial state and current state, respectively.

The deviatoric stress q is defined as:

$$q = \frac{h\bar{f}}{V} \tag{22}$$

where $\bar{f}$ is the force applied to loading plate. The mean effective stress p equals to:

$$p = \sigma_c + q/3 \tag{23}$$

4 Calibration of modeling parameters in DEM

The calibration of modeling parameters is an essential step of the DEM simulation. To ensure more realistic and reasonable numerical results, a systematic calibration framework is proposed in this section. The modeling parameters involved in the proposed DEM simulation are carefully classified and calibrated. The following sections will introduce the detailed procedures for the determination of all modeling parameters, which are required in DEM simulation.

4.1 Summary of modeling parameters and calibration process

In this section, we first present a summary of the proposed calibration framework to determine the modeling parameters that are required in the DEM simulations of rock clasts. According to the adopted contact models and the simulated material properties, the modeling parameters are divided into three groups, e.g., known parameters, measured parameters, and calculated parameters, as shown in Fig. 16.

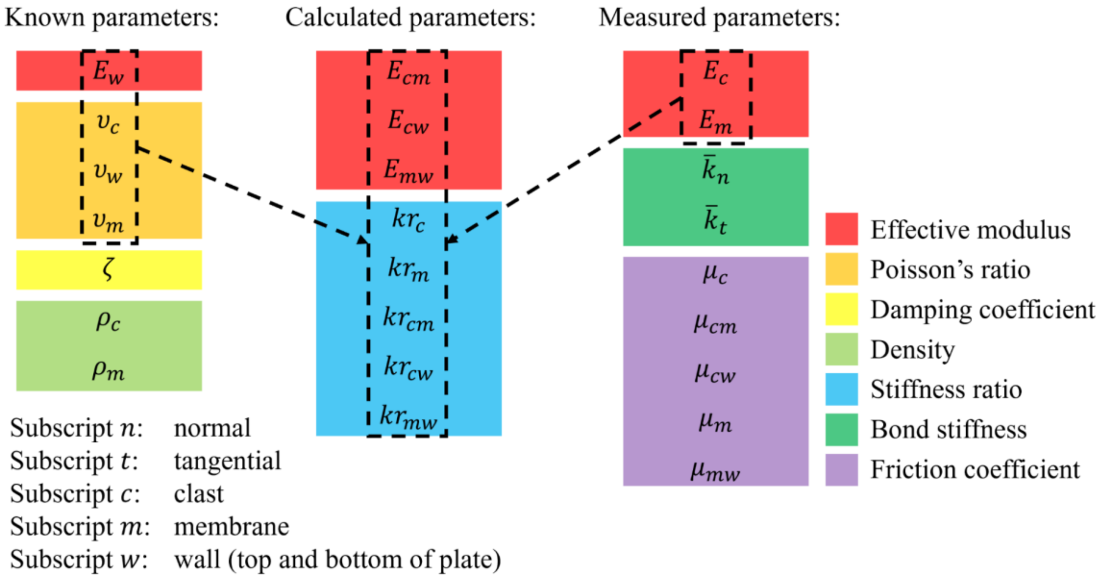

Fig. 16 Classification of parameters

4.1.1 Known parameters

The known parameters, including the effective modulus of wall E_w, Poisson's ratios υ_c, υ_m, υ_w, damping coefficient ζ, the density of clast ρ_c and membrane ρ_m, can be directly inferred from the intrinsic properties of the corresponding materials and the previous literature. The adopted values of the five known parameters are listed as follow:

(*a*) According to the manufacturer of triaxial apparatus, the effective modulus of wall E_w and Poisson's ratio of wall υ_w are 206 GPa and 0.3. The adopted values are also in line with the Chinese Design Code of Steel Structure (China 2017).

(*b*) The Poisson's ratio of clast υ_c is set to 0.25 according to the experimental study of similar rock clast in (Blake et al. 2019). The Poisson's ratio of rubber membrane υ_m is equal to 0.48 considering the extremely small volume compressibility of rubber (Lopera Perez et al. 2017).

(*c*) The damping coefficient ζ is set to 0.5 based on the previous DEM simulations in (Qu et al. 2019). It worth noted that, as suggested in (Nie et al. 2020), the ζ has low impact on the numerical results under the quasi-static condition.

(*d*) The density of clast ρ_c and membrane ρ_m are set to 2710 kg/m^3 and 809 kg/m^3 according to the real density of clast and membrane.

4.1.2 Measured parameters

The measured parameters include the effective modulus of clast E_c and membrane E_m, the normal $\bar{k}_n$ and tangential $\bar{k}_t$ bond stiffness, and the friction coefficients of clast-clast contact μ_c, membrane-membrane contact μ_m, clast-membrane contact μ_{cm}, clast-wall contact μ_{cw}, membrane-wall contact μ_{mw}. These parameters are expected to be measured from a series of calibration tests by approximating the DEM simulated results to the laboratory experimental ones. The detailed procedure of each calibration test will be introduced in the later sections.

4.1.3 Calculated parameters

The calculated parameters are computed based on the results of the known and measured parameters. There are eight calculated parameters, including three effective moduli of clast-membrane contact E_{cm}, clast-wall contact E_{cw}, membrane-wall contact E_{mw} and five stiffness ratios of clast-clast contact kr_c, membrane-membrane contact kr_m, clast-membrane contact kr_{cm}, clast-wall contact kr_{cw}, membrane-wall contact kr_{mw}.

Among them, the stiffness ratios can be directly calculated based on the corresponding Poisson's ratios for each contact type according to previous investigation (Li et al. 2017):

$$kr_* = \frac{2 - \upsilon_*}{2(1 - \upsilon_*)} \tag{24}$$

where the subscript $*$ denotes the contact type. It worth noted that, according to Eq. (24), the kr_c and kr_m can be directly calculated as 1.167 and 1.46, respectively. As for kr_{cm}, kr_{cw} and kr_{mw}, their corresponding υ_{cm}, υ_{cw} and υ_{mw} are required to be solved according to the following equation:

$$\upsilon_{12} = \frac{\upsilon_2 E_1(1 + \upsilon_2) + \upsilon_1 E_2(1 + \upsilon_1)}{E_1(1 + \upsilon_2) + E_2(1 + \upsilon_1)} \tag{25}$$

where the subscripts 1 and 2 denote the contact between material 1 and material 2. Among the parameters at the right-hand side of Eq. (25), the E_w, υ_c, υ_m, υ_w are known parameters while the E_c, E_m will be determined from the calibration tests in the later section.

Besides, the three effective moduli E_{cm}, E_{cm}, E_{cw} are calculated based on the following equation:

$$E_{12} = \frac{2E_1 E_2(2 - \upsilon_{12})(1 + \upsilon_{12})}{E_1(2 - \upsilon_2)(1 + \upsilon_2) + E_2(2 - \upsilon_1)(1 + \upsilon_1)} \tag{26}$$

It worth noted that Eq. (25) and Eq. (26) are derived from (Itasca 2014) based on the elastic theory.

According to the above-detailed classification of the modeling parameters and their relationships, the proposed calibration framework is given in Fig. 17. First, according to the material properties, we can easily obtain the known parameters. Then, based on a series of calibration tests on membrane and rock clasts, we can acquire most of the measured parameters, except the effective modulus of clast E_c. Next, a series of large triaxial compression test (with various trial values of E_c) are conducted to obtain the value of E_c. The macroscopic response of the numerical models is compared with that of the real experimental specimen to determine the precise value of E_c. Finally, all the calculated parameters can be solved based on the known parameters and the measured parameters.

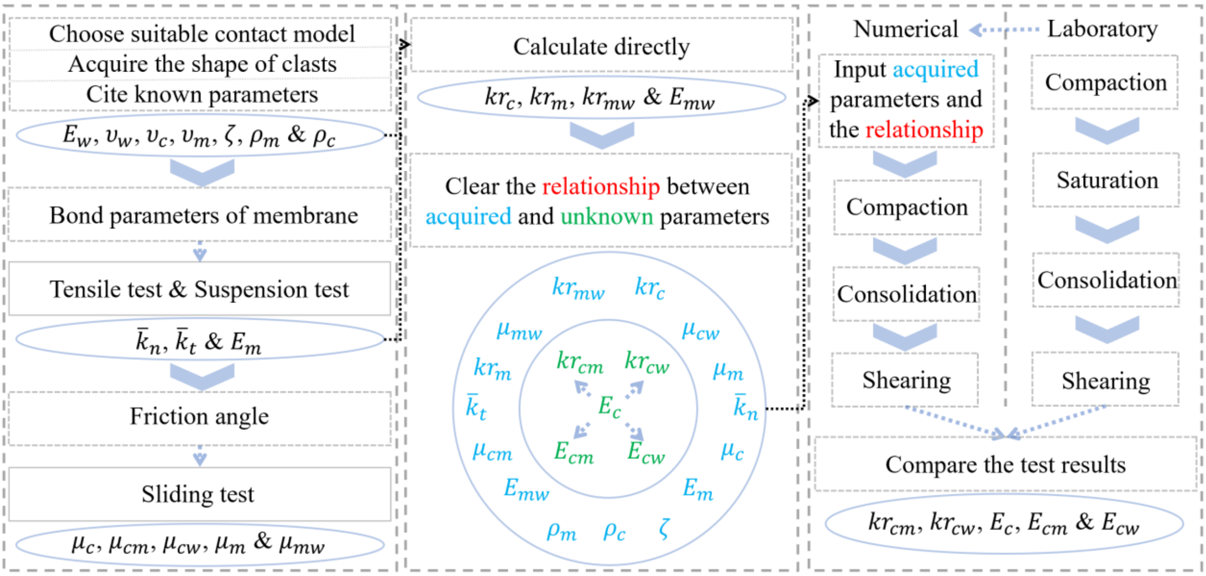

Fig. 17 The proposed framework for calibration of modeling parameter

4.2 Calibration of the membrane properties

In order to ensure that the behavior of the simulated membrane mimic the real boundary condition in the large triaxial compression test, the measured parameters, including $\bar{k}_n$, $\bar{k}_t$ and E_m, are carefully calibrated from a series of tensile tests and suspension tests.

As shown in Fig. 18 (*a*), a high precision tension testing system (MTS insight 30) is employed to conduct the tensile test of the rubber membrane. The tested rubber membrane is 75.0 mm in length, 22.0 mm in width, and 2.5mm in thickness. The simulation of the rubber membrane tensile test is conducted based on the following steps:

(1) First, the clustered-based bonded particle model of the rubber membrane with the same dimension

as the tested sample in the laboratory experiment is generated. The trial values of $\bar{k}_n$ and $\bar{k}_t$ are assigned to the membrane model.

(2) Then, two walls are generated to bond the top and bottom portions of the simulated membrane. The normal and tangential bond stiffness between walls and membrane particles is set to 10^5 times of $\bar{k}_n$ and $\bar{k}_t$, respectively.

(3) Next, the bottom wall is kept static and a constant upward velocity is applied on the top wall to pull up the membrane until a small strain increment is reached. This process is similar to the laboratory tensile test.

(4) The model is kept cycling until that the unbalanced force ratio (ratio of the mean unbalanced force to the mean contact force) is smaller than 10^{-10}.

(5) The elastic modulus of the membrane according to the size of the sample, the measured bonding force, and displacements of the top and bottom walls are computed. Finally, the elastic modulus of the membrane is recorded.

As shown in Fig. 18 (*b*), the suspension test is conducted by fixing the one side (20 mm in length) of the membrane at the horizontal plane and suspend another side (100 mm in length) of the membrane under gravity. The vertical displacement of ten measure points is recorded in the laboratory test. The process of the numerical suspension test is summarized as follow:

(1) Generate the cluster-based membrane model with the same dimension as the tested one and assign the trial values of $\bar{k}_n$ and $\bar{k}_t$.

(2) Fix the bonded particles on one side (20 mm) of the simulated membrane. Set gravity in the model and keep the model cycling until the unbalanced force ratio is less than 10^{-10}.

(3) Record the vertical displacement of all bonded particles. Compute the vertical displacement of the

measure points (same locations as the experimental ones) in the numerical model.

The above-described two calibration tests are performed iteratively to determine the bond stiffness $\bar{k}_n$ and $\bar{k}_t$. The adopted values of $\bar{k}_n$ and $\bar{k}_t$ are confirmed when the following two conditions are satisfied:

(1) The deviation of the elastic modulus of the membrane between the laboratory tensile test and the DEM simulation is smaller than 2%.

(2) The average deviation of the recorded vertical displacements between the measured points on the numerical model and laboratory specimen is smaller than 2%.

Based on these two criteria, the $\bar{k}_n$ and $\bar{k}_t$ are finally determined as 3.4×10^8 Pa/m and 2.4×10^8 Pa/m, respectively. As shown in Fig. 18 (*c*), using the calibrated $\bar{k}_n$ and $\bar{k}_t$, the simulation results are compared with the laboratory test results. It can be seen from the figures that both the stress-strain curve in the tensile test and the vertical displacement profile in the suspension test of the DEM simulation are consistent with those measured from the laboratory test. In addition, the effective modulus of membrane-membrane contacts E_m can be measured to be equal to 1.06MPa from the laboratory test. Subsequently, the membrane-wall parameters E_{mw} and kr_{mw} can be calculated as 1.06 MPa and 1.46 using Eq. (25) and (26), respectively.

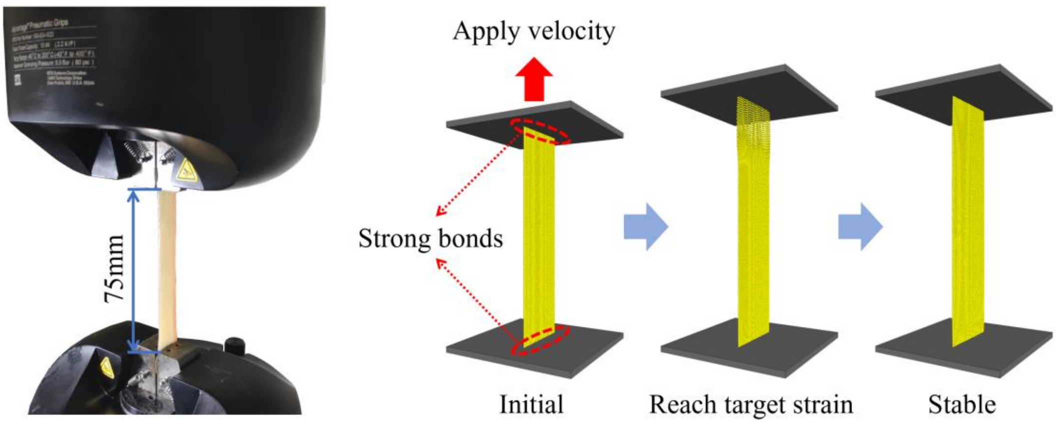

(a)

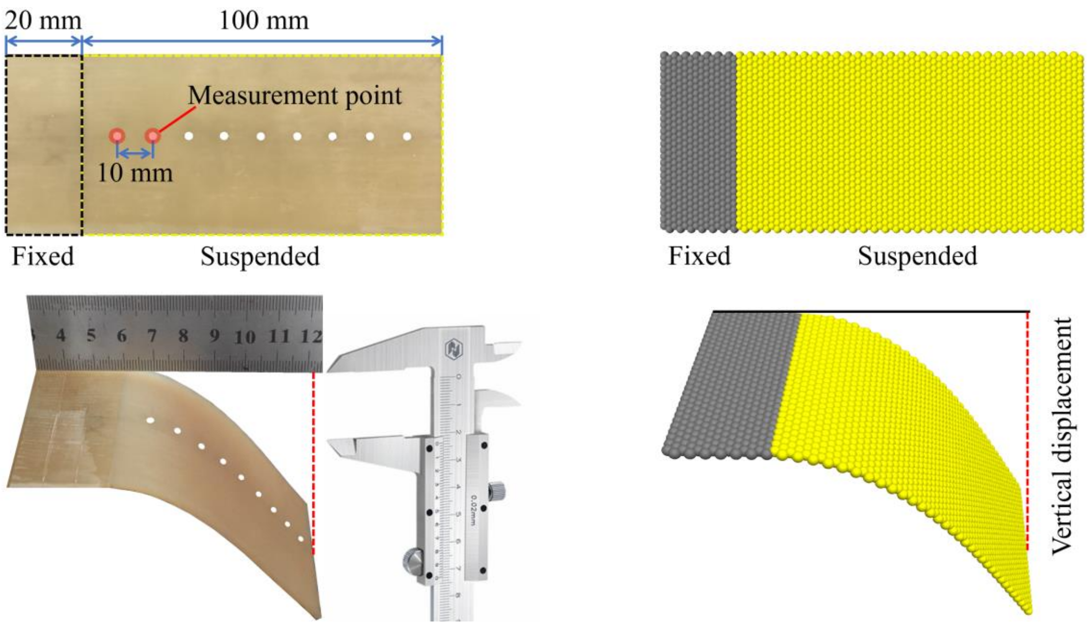

(b)

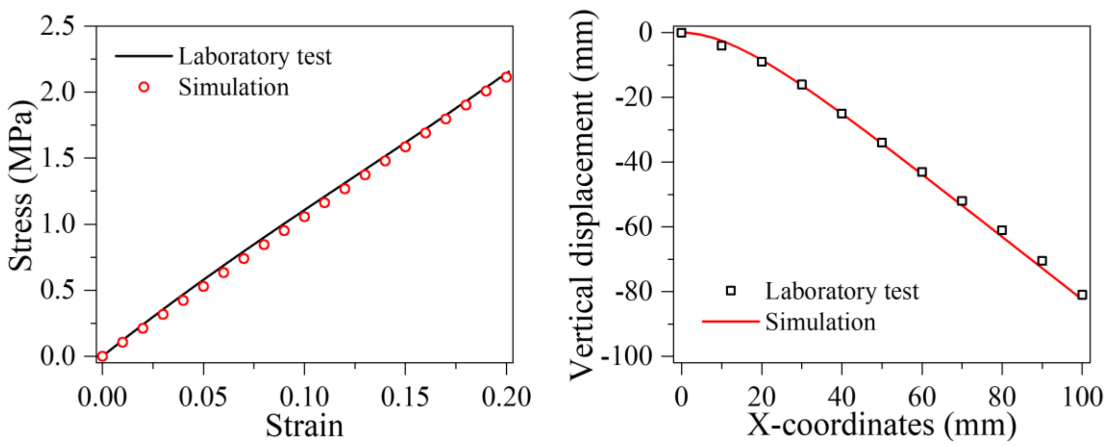

(c)

Fig. 18 Calibration of bond parameters: (a) tensile test, (b) suspension test and (c) test results

4.3 Calibration of friction coefficients

The friction coefficients between different materials have significant influences on the mechanical behaviors in DEM simulation. However, how to accurately determine the friction coefficients between various numerical objects is still a changeling task in DEM (Asadi et al. 2018b; Wang et al. 2018). In this study, a series of sliding tests are conducted to determine all the involved friction coefficients between clasts, the membrane, and the steel plate. An example is illustrated in Fig. 19 (*a*), for the friction coefficient between two contacted objects (A and B), the calibration process based on the sliding test in laboratory is performed as follows:

(1) Fix object A on a slope, and keep its upper surface parallel to the slope.
(2) Place object B on the upper surface of object A. Gradually increase the inclination of the slope and record the incline angle α when the upper object slips off.
(3) Generate the same numerical model of the corresponding laboratory sliding test in DEM. Ensure that the inclination angle of the interface between the two objects in the DEM model is the same as the recorded value α in the laboratory sliding test.
(4) Assign a trial value of the friction coefficient between the two objects and activate the gravity. Fix object A and run the DEM model.
(5) Gradually decrease the friction coefficient until object B slipped off in DEM. Record the updated friction coefficient when the slippage occurs.
(6) Conduct 20 tests following steps (1) - (5) to obtain more reliable results. It worth noted that for calibration of μ_c, μ_{cm}, and μ_{cw}, the tested rock clasts that have flat surfaces are carefully selected for each simulation.

Based on the above-described approach, the friction coefficients between clasts, membrane, and steel plate can be calibrated. Fig. 19 (*b*) – (*f*) illustrate the results of the experimental inclination angle and the simulated friction coefficient for each pair of target objects. It can be seen from the figures that for smooth contact interface conditions, e.g., wall (steel plate)-membrane contact and membrane-membrane contact, the recorded incline angles and friction coefficients have relatively smaller deviations, while the results of clast-clast contact show the largest fluctuation. Based on the calibrated tests, the average friction coefficients for each contact types are adopted as $\mu_{cm} = 0.65$, $\mu_c = 0.97$,

$\mu_m = 0.9$, $\mu_{mw} = 0.64$ and $\mu_{cw} = 0.43$.

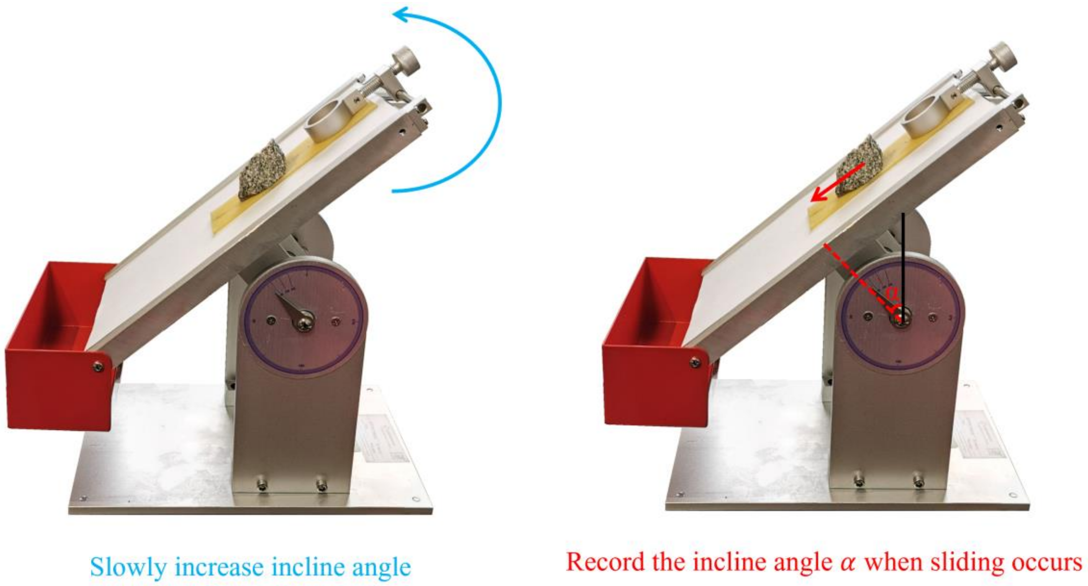

(a)

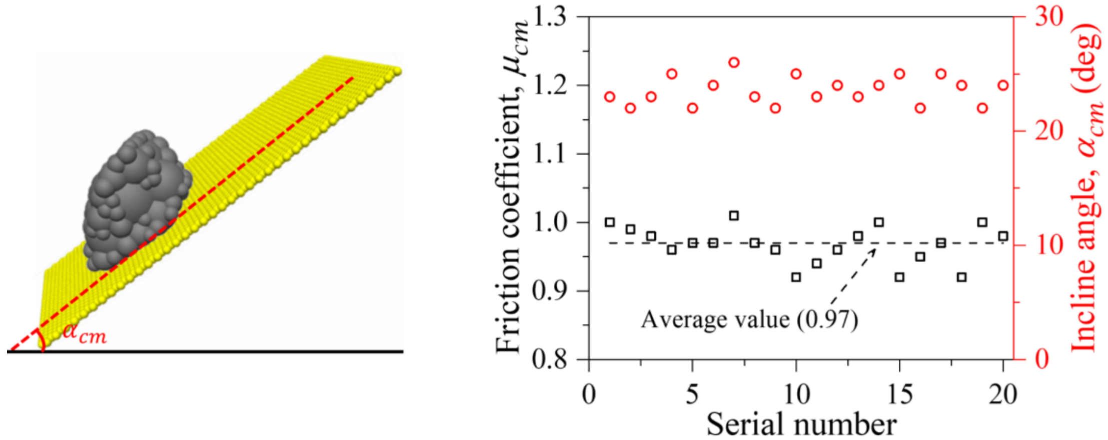

(b)

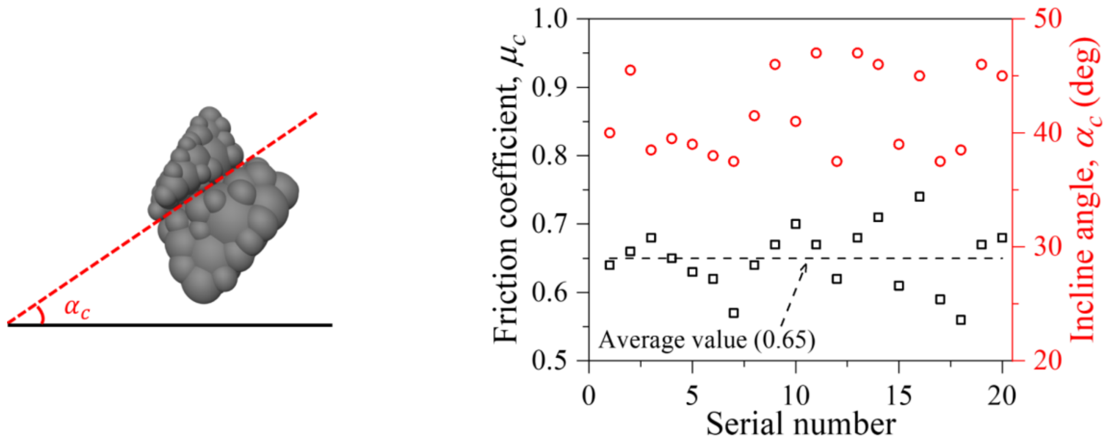

(c)

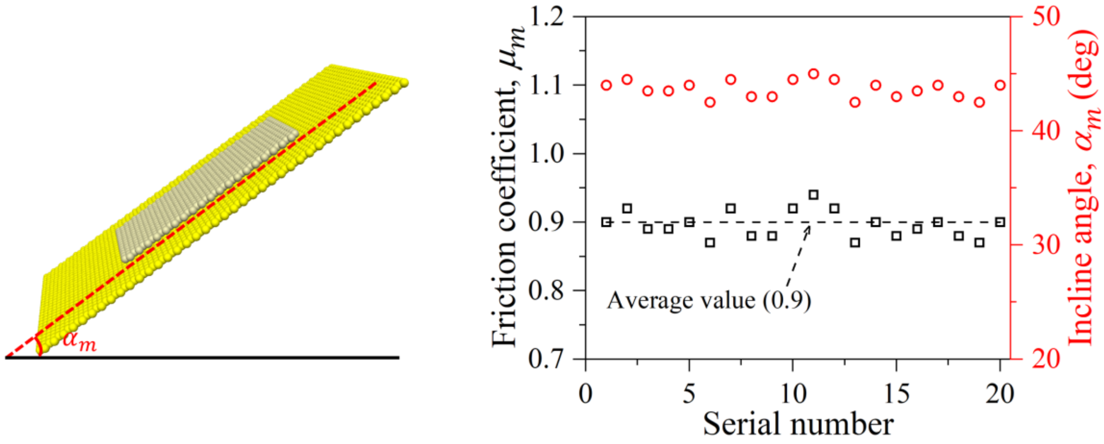

(d)

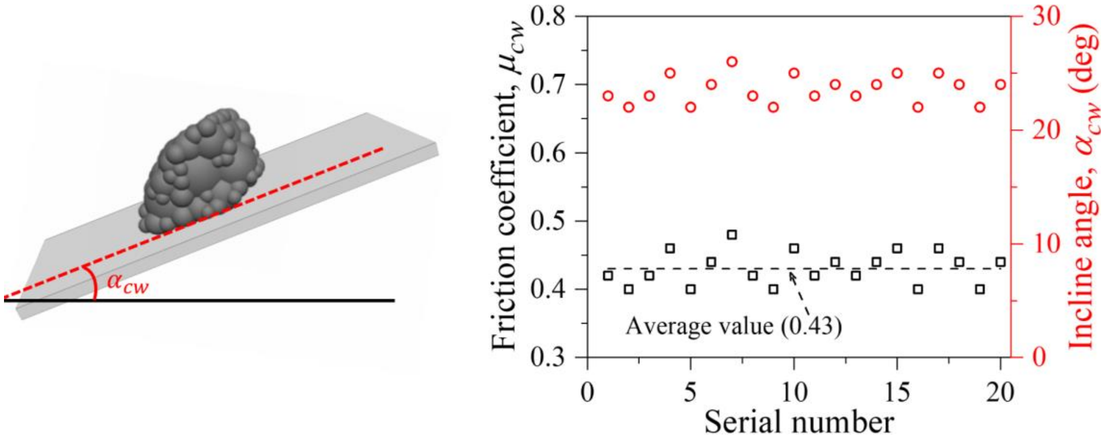

(e)

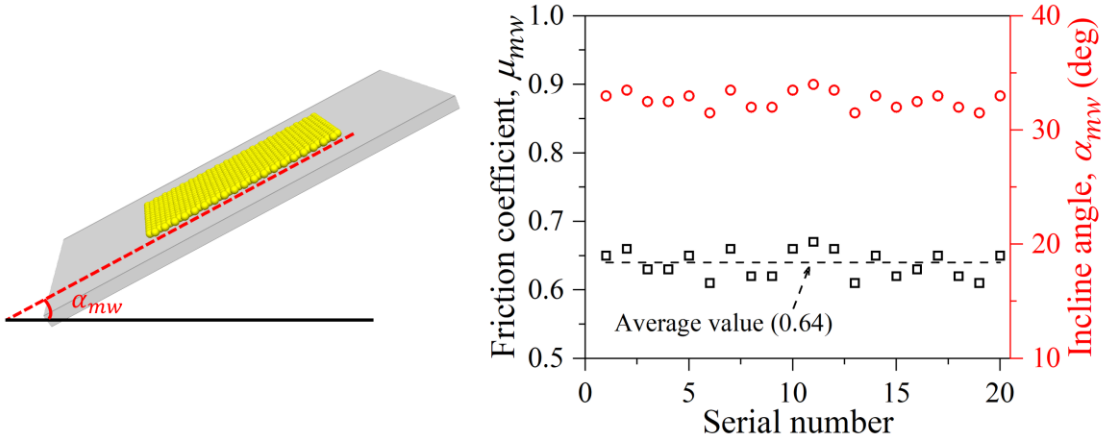

(f)

Fig. 19 Sliding test: (a) method and (b) results

4.4 Calibration of effective modulus

The last modeling parameter that is required to be calibrated is the effective modulus of clast-clast contact E_c. In this study, a series of laboratory triaxial compression tests of rock clasts are conducted and the macroscopic behaviors, e.g., stress-strain relationship, the volume change, are employed as the benchmarks for calibration of E_c in DEM. The procedure to calibrate E_c based on the laboratory tests and DEM simulations are detailed as follow:

(1) Prepare five specimens of rock clasts with the same particle size distribution (as shown in Fig. 2) for laboratory tests. All the specimens are compacted to reach the target degree of compaction equal to 95% (about 0.56 in the void ratio). The dimension of each cylindrical specimen is 600 mm in height and 300 mm in diameter. The maximum particle size of the tested rock clasts is limited to 50.0 mm so that the size ratio between the particle and specimen reaches 1:6 according to the suggestion in ASTM and previous investigations (Indraratna et al. 2011; Marschi et al. 1972).

(2) Conduct the large-scale triaxial compression tests on the five specimens following the detailed process introduced in section 3.4. For each test, the confining pressure σ_c is set as 50kPa to prevent the clasts from breakage. The shear strain rate is maintained at 2 mm/min during the triaxial compression test. The tests are completed when the 15% axial strain is achieved. It worth noted that crushed clasts are rarely found after testing, which indicated that the non-breakage assumption is suitable in this study.

(3) According to the conventional range of effective modulus of rock clast in the previous investigations (Gong et al. 2019a; Sun et al. 2018), put forward a series of trial values of E_c and compute the remaining relevant modeling parameters E_{cw}, kr_{cw}, E_{cm}, kr_{cm}. Input all modeling parameters into DEM to simulate the large-scale triaxial compression tests following the detailed process introduced in section 3.4.

(4) Compare the results of the deviatoric stress and volumetric strain between the experimental tests and the numerical simulations. Select the most appropriate value of E_c so that the numerical output has the best goodness of fitting with the macroscopic behaviors of rock clasts in the experimental tests.

As shown in Fig. 20, three example results of the numerical simulations (with E_c = 0.2 GPa, 2.0 GPa and 20 GPa) are compared with the laboratory results. It can be seen from the figure that larger E_c leads to significant higher shear stiffness and larger shear strength. In addition, the trend of dilatancy is also positively correlated with the adopted E_c. Since the numerical model with E_c = 2.0 GPa shows satisfied fitness to the experimental results, we adopt E_c = 2.0 GPa in this study and remaining calculated parameters can also be determined as E_{cw} = 1.98 GPa, $kr_{cw} = 1.167$, E_{cm} = 2.12 kPa, kr_{cm} = 1.46.

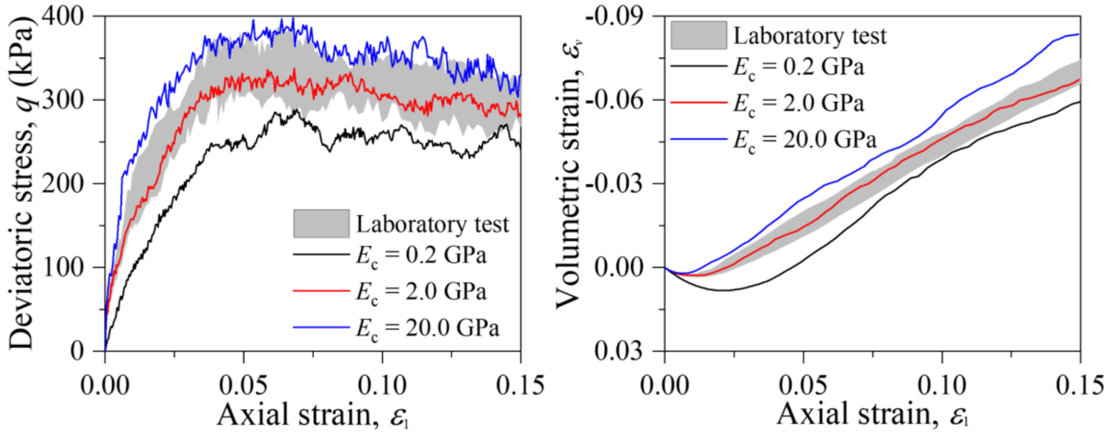

(a) (b)

Fig. 20 Comparison of typical mechanical responses in the triaxial test under a confining pressure of 50 kPa: (a) deviatoric stress and (b) volumetric strain

4.5 Influence of gravity in homogeneity

The large triaxial specimen is heavy and, in consequence, the inhomogeneity of specimen caused by gravity may be larger. Thus, it is necessary to analyze the gravity induced inhomogeneity.

First, the visualized contact force network at ε_1 = 0% and ε_1 = 15% is compared in Fig. 21 (*a*). At the beginning of shearing, the density of strong contact force (red line) near the base plate is greater than that near the loading plate because of the wight of clasts. But this phenomenon is not obvious at the end of shearing. This difference relates to the fact that the influence of gravity in homogeneity highly depends on the mean effective stress *p*.

To accquire the influence of gravity in micro perspective, the average stress tensor of a single particle $\bar{\sigma}_{ij}^{P}$ which was given by Potyondy and Cundall (Potyondy and Cundall 2004) is introduced:

$$\bar{\sigma}_{ij}^{P}=\frac{1}{V^{P}}\sum_{C=1}^{N_{CP}} f_i^C r_j^C \tag{27}$$

where V^P is the volume of the given particle, N_{CP} is the contact number of the given particle, f_i^C is the i^{th} component of the contact force, and r_j^C is the j^{th} component of the vector connecting the contact point to the particle center.

According to the position of particles in specimen (Fig. 21b), the particle stress ratio *PSR*, which may be a persuasive index to reflect the gravity induced inhomogeneity in micro perspective, is defined as:

$$PSR=\frac{\text{Average } \bar{\sigma}_{zz}^{P} \text{ in top zone}}{\text{Average } \bar{\sigma}_{zz}^{P} \text{ in bottom zone}} \tag{28}$$

As shown in Fig. 21 (*b*), the particle stress ratio *PSR* increases to a plateau during shear. Combine to the development of deviatoric stress in Fig. 20 (*a*), we can conclude that the difference of particle stress in top zone and bottom zone gradually decreases with increasing *p*. In other words, the increasing *p* leads to the decreasing influence of gravity in homogeneity. It should be noted that the value of plateau of *PSR* is larger than 1.0. This result indicates that the particles in top zone have higher probability to participate in the strong contact force chain compare to the particles in bottom zone, consistent with the density of strong contact force observed in Fig. 21 (*a*).

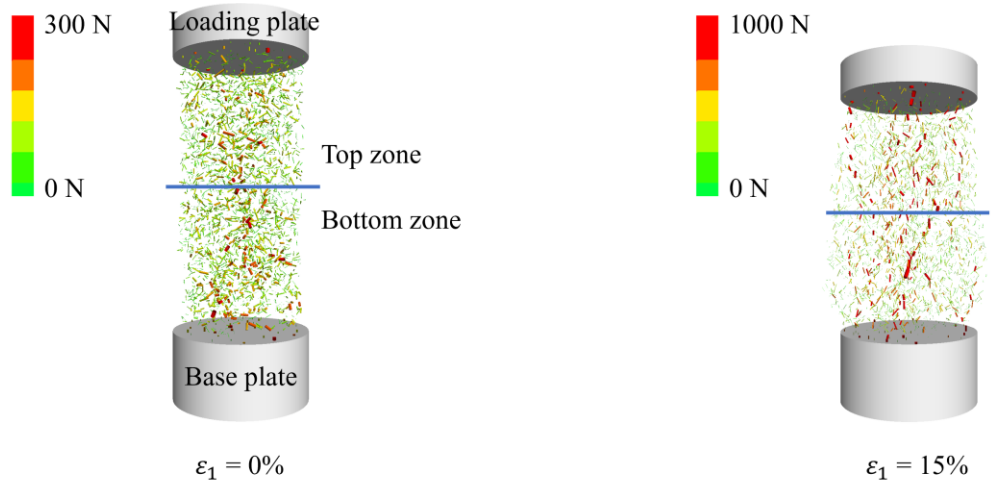

(a)

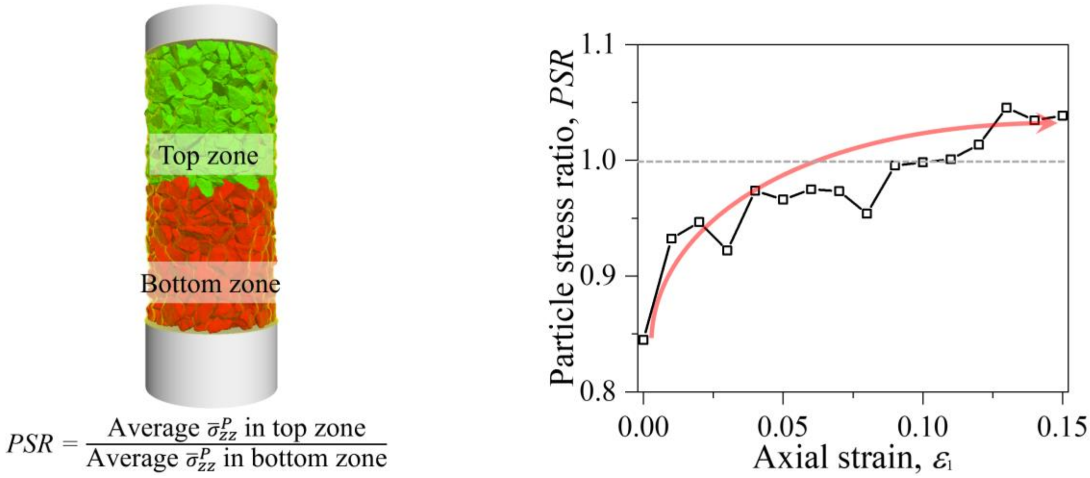

(b)

Fig. 21 Gravity induced inhomogeneity of contact force (a) visualized contact force network and (b) particle stress ratio

5 Application and analysis

To further illustrate the capability of the proposed method, the DEM simulations of large scale triaxial compression tests are performed to investigate the macro-and micro-mechanical behaviors of rock clasts under different confining pressure conditions. All the adopted modeling parameters are obtained from the above-described calibration tests and are summarized in Table 1.

Table 1 Material properties used in the DEM simulation

Type	Parameter	Value
Linear elastic model	Effective modulus of clast-clast contacts, E_c (Pa)	2.0×10^9
	Effective modulus of clast-membrane contacts, E_{cm} (Pa)	2.12×10^6
	Effective modulus of clast-wall contacts, E_{cw} (Pa)	1.98×10^9
	Effective modulus of membrane-membrane contacts, E_m (Pa)	1.06×10^6
	Effective modulus of membrane-wall contacts, E_{mw} (Pa)	1.06×10^6
	Stiffness ratio of clast-clast contacts, kr_c	1.167
	Stiffness ratio of clast-membrane contacts, kr_{cm}	1.46
	Stiffness ratio of clast-wall contacts, kr_{cw}	1.167
	Stiffness ratio of membrane-membrane contacts, kr_m	1.46
	Stiffness ratio of membrane-wall contacts, kr_{mw}	1.46
Simplified parallel bond model	Normal stiffness of parallel bond, $\bar{k}_n$ (Pa/m)	3.4×10^8
	Tangential stiffness of parallel bond, $\bar{k}_t$ (Pa/m)	2.4×10^8
Friction coefficient	Friction coefficient of clast-clast contacts, μ_c	0.65
	Friction coefficient of clast-membrane contacts, μ_{cm}	0.97
	Friction coefficient of clast-wall contacts, μ_{cw}	0.43
	Friction coefficient of membrane-membrane contacts, μ_{mm}	0.9
	Friction coefficient of membrane-wall contacts, μ_{mw}	0.64
	Density of clast, ρ_c (kg/m^3)	2710
	Density of membrane particles, ρ_m (kg/m^3)	809
Global parameter	Damping coefficient, ζ	0.5

The range of the confining pressure is similar to the measured value in the ballast layer of the heavy haul railway (Sun et al. 2019). It worth noted that the influence of particle breakage is eliminated since the rock aggerates are modeled as non-breakage clump particles. The initial fabric properties, e.g., spatial arrangement and orientations of the rock clasts, are kept as the same to ensure that the confining pressure is the only variable in this numerical study.

As shown in Fig. 22, all preshear specimens are made from one compacted specimen. To eliminate the effect of gravity induced inhomogeneity, the consolidation and shearing process is in non-gravity condition (Shire and O'Sullivan 2012). Moreover, both loading plate and base plate move to each other in same velocity during shear. Four different confining pressure (e.g., 12.5 kPa, 25 kPa, 50 kPa, 100 kPa) are activated with the simulated rubber membrane considering the non-breakage assumption. After the consolidated specimens are obtained, all samples are sheared to the same axial strain (ε_1=15%). It can be observed from Fig. 22 that the surface of sheared specimens became more rugged with the increasing confining pressure. This phenomenon indicates that the decreased preshear void ratios of specimens (shown in Fig. 22) highly relates to the distortion of rubber membrane according to the confining pressure.

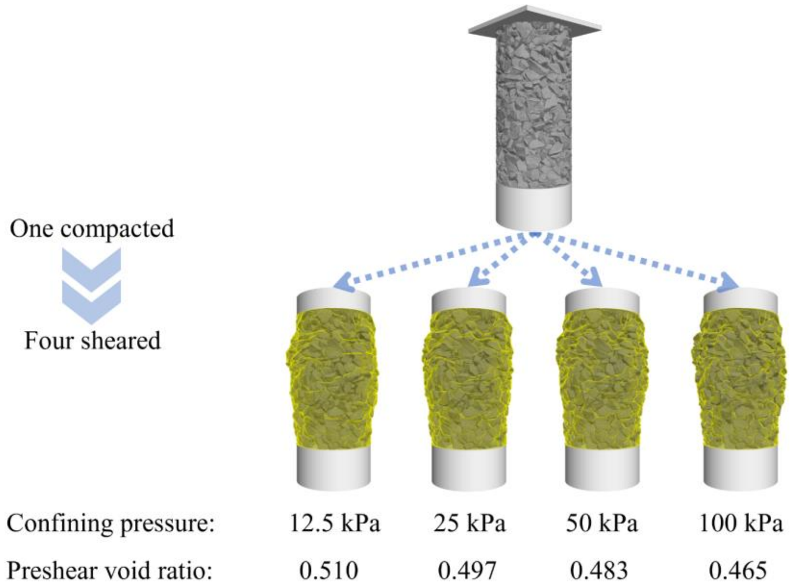

Fig. 22 Simulation schemes

The results of numerical triaxial tests are analyzed from both macroscale and microscale perspectives. In the macroscale perspective, we focus on shear strength and dilatancy. The microscale analysis is divided into inter-particle structure and contact behaviors. The evolutions of mean coordination number, particle orientation, connectivity, and sliding contact during the shear process are investigated to explain the macroscale response. Moreover, the shear band is analized based on the displacement and rotation of particles.

5.1 Shear strength and dilatancy

As shown in Fig. 23, the typical outputs of triaxial tests in compression, including the stress ratio - axial strain curves and the volumetric strain - axial strain curves, are computed. It can be seen from Fig. 23 (*a*) that the stress ratios of all samples gradually increase to a plateau versus the increasing axial strain. With increasing confining pressure σ_c, both the peak stress ratio and the shear modulus become smaller. Fig. 23 (*b*) displays the shear-induced dilatancy. In general, all specimens undergo an initial slight contraction and then exhibit significant dilation. With increasing σ_c, the volumetric dilatancy of the specimen is smaller.

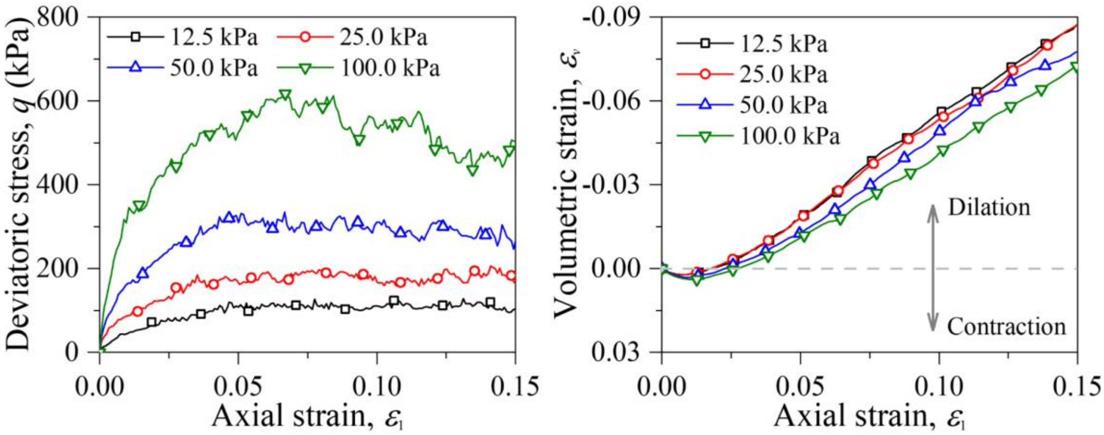

(a) (b)

Fig. 23 Typical curves in triaxial test: (a) stress ratio and (b) volumetric strain

5.2 Inter-particle structure

The mean coordination number $CN_{P,}$ and the orientation distributions are studied to reveal the evolution of inter-particle structures during shear.

The mean coordination number CN_P is defined as the average number of neighboring clast particles. The CN_P can indicate the particle rearrangement and the internal packing structure. As shown in Fig. 24, as expected, CN_P increases with increasing confining pressure. In addition, during shear, CN_P of all specimens sharply increases in $\varepsilon_1 \in$ (0, 0.01), and then slowly decrease to a plateau. The result demonstrates that the inter-particle structure becomes denser during the initial shear stage, which is consistent with the phenomena observed from the volumetric strain curve.

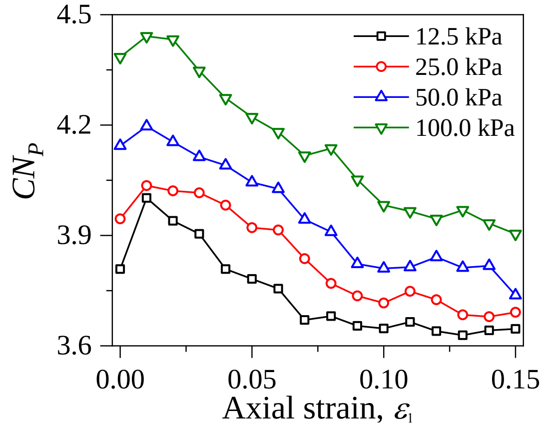

Fig. 24 The coordination number of clast particles *CN_P*

The orientation distributions are visualized on the horizontal and vertical planes, as shown in Fig. 25. It can be seen from the figure that the orientation distributions in x-z plane and y-z plane are very similar. The dotted line and solid line indicate the orientation distributions of compacted specimens and sheared specimens, while the grey dotted line represents the compacted state of the sample before the consolidation process. Obviously, the major principal orientations of clasts mainly accumulated near the horizontal plane in all stages. It is easy to understand that an clast is more likely to align perpendicular to the gravitational directions to reach a stable state. The orientation distributions of rock clasts show obviously preferable directions before shear, indicating that the process of compaction leads to significant fabric anisotropy. After applying confining pressure in the rubber membrane, the anisotropy decreases. Moreover, the shearing process also results in increasing anisotropy. However, the influence of confining pressure on the anisotropy of clast orientation is negligible in the range of this study.

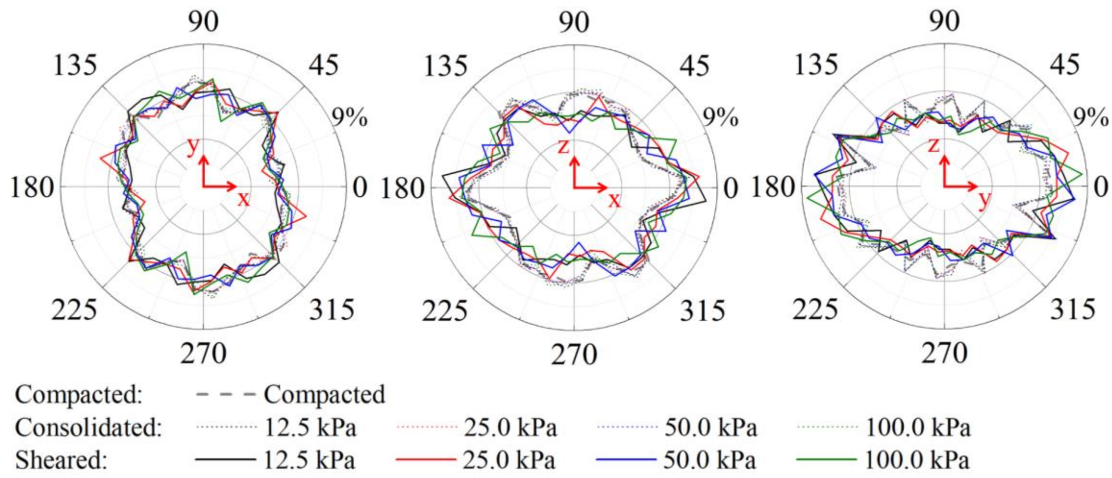

(a) (b) (c)

Fig. 25 Statistic of the direction of clast: (a) in x-y plane, (b) in x-z plane and (c) in y-z plane

5.3 Contact behaviors

In this section, the contact behaviors are characterized by the percentage of the particles with connectivity larger than 4, *P*(*C*≥*4*), and the percentage of sliding contact, S_p.

Connectivity *C* is the contact number for a specific particle (Nie et al. 2019). In three dimensions, particles with *C*≤*3* cannot contribute to stability. Thus, the percentage of particles with connectivity *C*≥*4*, *P(C*≥*4)*, can reflect the internal stability of specimens under external load. Fig. 26 (*a*) displays the evolution of *P(C*≥*4)* during shear at a different confining pressure σ_c. Increasing σ_c leads to a distinct increase in *P(C*≥*4)*. This can be easily understood as higher σ_c makes the specimens denser and more stable. Moreover, for a specific σ_c, *P(C*≥*4)* initially increases to a peak, and then gradually decreases to a plateau. Compare the trend of *P(C*≥*4)* and ε_v, we can conclude that the most stable conditions of the specimens appear after the initial contraction, and the specimens gradually become unstable as the dilatancy becomes larger.

The evolution of the percentage of sliding contact S_P during shear is presented in Fig. 26 (*b*). In general, S_P first increases to a peak and then gradually decreases, indicating that the sliding between clasts diminishes with tangential and normal contact force become more and more important. In addition, the larger the confining pressure is, the smaller the S_P is. This phenomenon indicates that the increasing confining pressure hinders the sliding and thus leads to a smaller dilatancy, as revealed in Fig. 23 (*b*).

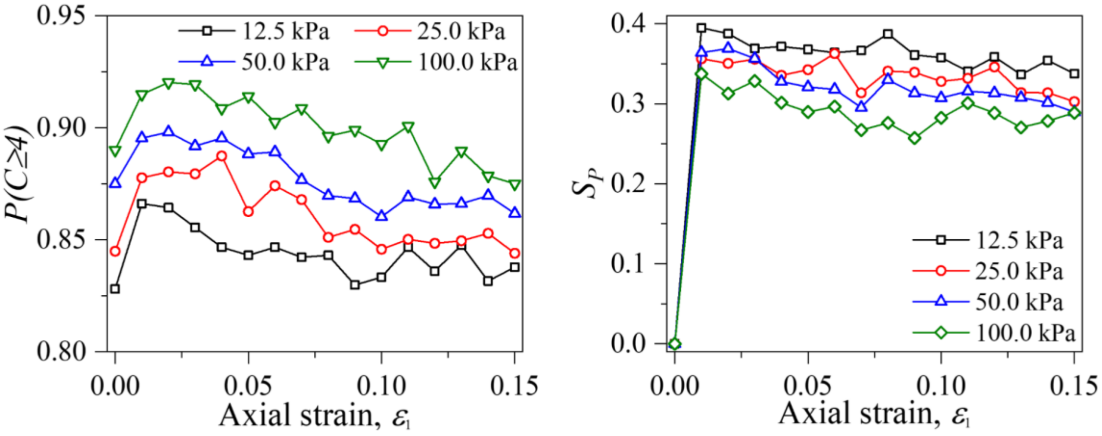

(a) (b)

Fig. 26 Quantification of contact behaviors: (a) percentage of particles with connectivity larger than 4 *P(C≥4)* and (b) percentage of sliding contact S_P of specimens

5.4 Shear band analysis

The shear band is a common feature of localisation plastic deformation for the instability of triaxial specimen. Compare to conventional servo method (e.g., wall-based servo method), one outstanding advantage of the membrane-based servo method is the realistic shear band (Qu et al. 2019). For wall-based servo method, the particles are forced to adapt to the kinematics of the boundary walls. But for membrane-based servo method, particles are able to move freely at any position. The shear band can be recognised by non-strain indications (Qu et al. 2019). Thus, in this section, particle displacement and particle rotation are selected to visualize and analyze the shear band.

Fig. 27 (*a*) illustrates the displacement of particles as vectors at ε_1 = 15%, and the thickness of vectors is scaled by magnitude. Obviously, the inclination of shear bands increase with increasing confining pressure σ_c. The localised instability may be dominated by strong local inhomogeneity (Rice 1976). In other words, the initial flaws (or relatively large voids) in the specimen give rise to concentrating deformation in its vicinity. Thus, the stronger contact force caused by the increasing σ_c leads to the larger development of the initial flaws. In consequence, the inclination of shear bands increase.

Fig. 27 (*b*) shows the distribution of cumulative rotation of particles ω at ε_1 = 15% which was proposed by Zhu et al. (Zhu and Yin 2019). Similar to particle size distribution, the rotational distribution is the volumetric (or mass) percentage of particles rotating to a greater degree than indicated by ω. The particles in triaxial specimen can be divided into low rotational, transmission and high rotational according to ω. All the curves of rotational distribution intersect at ω = 0.28 radians. The particles with ω $\leq$0.28 radians can be named as low rotational particles which are not engaged in shear band. It can be concluded from the results that higher σ_c leads to fewer percentage of low rotational particles, indicating that the area of shear band increases with increasing σ_c.

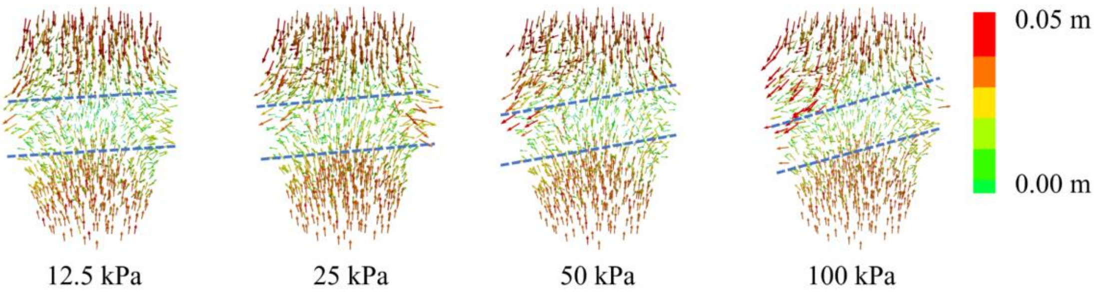

(a)

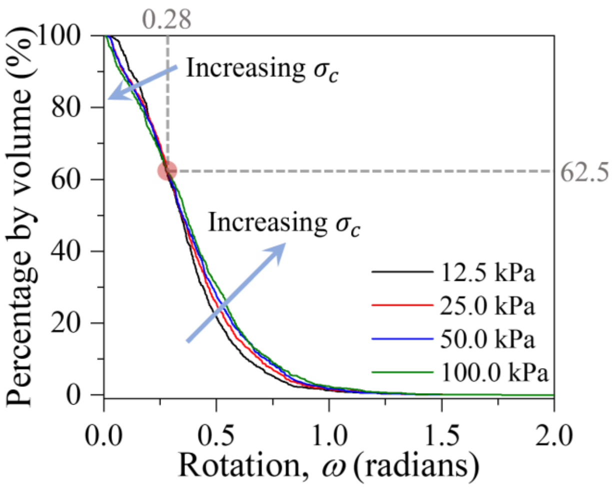

(b)

Fig. 27 Shear band analysis: (a) visualization of shear band at ε_1 = 15% and (b) distribution of particle rotation

6 Conclusion

A DEM modeling framework of the large scale triaxial test on rock clasts has been proposed with a systematic calibration process. The fitness between numerical simulations and laboratory test results in both stress ratio and volumetric strain indicated that the proposed method is reliable. Furthermore, the proposed method is applied to investigate the macro- and microscopic behaviors of rock clasts under different confining pressures. The main contributions of the proposed study are summarized as follows:

(1) Close-range photogrammetry is employed to reconstruct the 3D particle model of the realistic rock clasts. The shapes of the sampled rock clasts are quantitatively analyzed, and the clump-based model is adopted to approximate the realistic particle morphology in DEM.

(2) The flexible boundary of the triaxial test in the real laboratory experiment is simulated as a cluster-based membrane model, which employs the simplified linear parallel bond model to bonded the neighboring particle elements in a triangular meshes network. Subsequently, the membrane servo control algorithm based on the cluster-based membrane model is developed in PFC3D$^{5.0}$ to activate

the confining pressure.

(3) A systematic procedure for calibration of modeling parameters is proposed to accurately capture the properties of the realitstic material in DEM simulation. The calibration tests include tensile and suspension tests (membrane properties), sliding tests (friction coefficients), and the large-scale triaxial compression tests (effective modulus).

(4) The proposed approach is employed to simulate the large scale triaxial compression tests of rock clasts with different confining pressures. The macroscopic quantities, including the mean coordination number, particle orientation, connectivity, and sliding contact, are analyzed to explain the evolution of the macroscale responses, e.g., shear strength and dilatancy.

Acknowledgments

References

Asadi, M., Mahboubi, A. & Thoeni, K. 2018a. Discrete modeling of sand-tire mixture considering grain-scale deformability. Granular Matter, **20**, 18, doi: 10.1007/s10035-018-0791-4.

Asadi, M., Thoeni, K. & Mahboubi, A. 2018b. An experimental and numerical study on the compressive behavior of sand-rubber particle mixtures. Computers and Geotechnics, **104**, 185-195, doi: 10.1016/j.compgeo.2018.08.006.

ASTM. 2011. Standard method for consolidated drained triaxial compression test for soils. ASTM D7181.

ASTM. 2012. Standard Test Methods for Laboratory Compaction Characteristics of Soil Using Modified Effort. ASTM D1557.

Barrett, P.J.S. 1980. The shape of rock particles, a critical review. **27**, 291-303.

Blake, O.O., Faulkner, D.R. & Tatham, D.J. 2019. The role of fractures, effective pressure and loading on the difference between the static and dynamic Poisson's ratio and Young's modulus of Westerly granite. International Journal of Rock Mechanics and Mining Sciences, **116**, 87-98, doi: 10.1016/j.ijrmms.2019.03.001.

Chang, C.S. & Yin, Z.-Y. 2010. Micromechanical Modeling for Inherent Anisotropy in Granular Materials. **136**, 830-839, doi: doi:10.1061/(ASCE)EM.1943-7889.0000125.

Cheng, H., Nakata, Y. & Bolton, M. 2003. Discrete Element Simulation of Crushable Soil. Cheng, Y.P. and Nakata, Y. and Bolton, M.D. (2003) Discrete element simulation of crushable soil. Géotechnique, 53 (7). pp. 633-641. ISSN 00168505, **53**, doi: 10.1680/geot.2003.53.7.633.

Cheung, G. & O'Sullivan, C. 2008. Effective simulation of flexible lateral boundaries in two- and three-dimensional DEM simulations. Particuology, **6**, 483-500, doi: 10.1016/j.partic.2008.07.018.

China, M.o.H.a.U.-R.C.o.t.P.s.R.o. 2017. Standard for Design of Steel Structures in China. GB50017-2017.

Farhang, B. & Mirghasemi, A.A. 2017. A study of principle stress rotation on granular soils using DEM simulation of hollow cylinder test. Advanced Powder Technology, **28**, 2052-2064, doi: 10.1016/j.apt.2017.05.011.

Gao, G. & Meguid, M.A. 2018. Effect of particle shape on the response of geogrid-reinforced systems: Insights from 3D discrete element analysis. Geotextiles and Geomembranes, **46**, 685-698, doi: 10.1016/j.geotexmem.2018.07.001.

Goldenberg, C. & Goldhirsch, I. 2005. Friction enhances elasticity in granular solids. Nature, **435**, 188-191, doi: 10.1038/nature03497.

Gong, H., Song, W., Huang, B., Shu, X., Han, B., Wu, H. & Zou, J. 2019a. Direct shear properties of railway ballast mixed with tire derived aggregates: Experimental and numerical investigations. Construction and Building Materials, **200**, 465-473, doi: 10.1016/j.conbuildmat.2018.11.284.

Gong, J. & Liu, J. 2017. Effect of aspect ratio on triaxial compression of multi-sphere ellipsoid assemblies simulated using a discrete element method. Particuology, **32**, 49-62, doi: https://doi.org/10.1016/j.partic.2016.07.007.

Gong, J., Nie, Z., Zhu, Y., Liang, Z. & Wang, X. 2019b. Exploring the effects of particle shape and content of fines on the shear behavior of sand-fines mixtures via the DEM. Computers and Geotechnics, **106**, 161-176, doi: 10.1016/j.compgeo.2018.10.021.

Han, B.Y., Ling, J.M., Shu, X., Gong, H.R. & Huang, B.S. 2018. Laboratory investigation of particle size effects on the shear behavior of aggregate-geogrid interface. Construction and Building Materials, **158**, 1015-1025, doi: 10.1016/j.conbuildmat.2017.10.045.

Hu, W., Yin, Z.-Y., Scaringi, G., Dano, C. & Hicher, P.-Y. 2018. Relating fragmentation, plastic work and critical state in crushable rock clasts. Engineering Geology, **246**, 326-336, doi: https://doi.org/10.1016/j.enggeo.2018.10.012.

Indraratna, B., Gasson, I. & Chowdhury, R.N. 2011. Utilization of compacted coal tailings as a structural fill. Canadian Geotechnical Journal, **31**, 614-623, doi: 10.1139/t94-074.

Indraratna, B., Tennakoon, N., Nimbalkar, S. & Rujikiatkamjorn, C. 2013. Behaviour of clay-fouled ballast under drained triaxial testing. Geotechnique, **63**, 410-419, doi: 10.1680/geot.11.P.086.

Itasca. 2014. User's manual for PFC3D. Itasca Consulting Group, Inc., Minneapolis, USA.

Koohmishi, M. & Palassi, M. 2016. Evaluation of the Strength of Railway Ballast Using Point Load Test for Various Size Fractions and Particle Shapes. Rock Mechanics and Rock Engineering, **49**, 2655-2664, doi: 10.1007/s00603-016-0914-3.

Koohmishi, M., Palassi, M.J.R.M. & Engineering, R. 2016. Evaluation of the Strength of Railway Ballast Using Point Load Test for Various Size Fractions and Particle Shapes. **49**, 2655-2664.

Li, X.q., Chen, Z.a., Zhang, L.t. & Jia, D. 2016. Construction and Accuracy Test of a 3D Model of Non-Metric Camera Images Using Agisoft PhotoScan. Procedia Environmental Sciences, **36**, 184-190, doi: https://doi.org/10.1016/j.proenv.2016.09.031.

Li, Y.Y., Cui, H.Q., Zhang, P., Wang, D.K. & Wei, J.P. 2020. Three-dimensional visualization and quantitative characterization of coal fracture dynamic evolution under uniaxial and triaxial compression based on mu CT scanning. Fuel, **262**, 11, doi: 10.1016/j.fuel.2019.116568.

Li, Z., Wang, Y.H., Ma, C.H. & Mok, C.M.B. 2017. Experimental characterization and 3D DEM simulation of bond breakages in artificially cemented sands with different bond strengths when subjected to triaxial shearing. Acta Geotechnica, **12**, 987-1002, doi: 10.1007/s11440-017-0593-6.

Liu, S., Qiu, T., Qian, Y., Huang, H., Tutumluer, E. & Shen, S. 2019. Simulations of large-scale triaxial shear tests on ballast aggregates using sensing mechanism and real-time (SMART) computing. Computers and Geotechnics, **110**, 184-198, doi: https://doi.org/10.1016/j.compgeo.2019.02.010.

Liu, Y., Zhou, X., You, Z., Yao, S., Gong, F. & Wang, H. 2017. Discrete element modeling of realistic particle shapes in stone-based mixtures through MATLAB-based imaging process. Construction and Building Materials, **143**, 169-178, doi: 10.1016/j.conbuildmat.2017.03.037.

Lopera Perez, J., Kwok, F. & Senetakis, K. 2017. Effect of rubber content on the unstable behaviour of sand-rubber mixtures under static loading: a micro-mechanical study. Geotechnique, 1-36, doi: 10.1680/jgeot.16.p.149.

Lu, M. & McDowell, G.R. 2006. The importance of modelling ballast particle shape in the discrete element method. Granular Matter, **9**, 69-80, doi: 10.1007/s10035-006-0021-3.

Marschi, N.D., Chan, C.K. & Seed, H.B. 1972. Evaluation of properties of rockfill materials. Journal of the Soil Mechanics and Foundations Division, **98**, 95-114.

Miao, C.-x., Zheng, J.-j., Zhang, R.-j. & Cui, L. 2017. DEM modeling of pullout behavior of geogrid reinforced ballast: The effect of particle shape. Computers and Geotechnics, **81**, 249-261, doi: 10.1016/j.compgeo.2016.08.028.

MiDi, G.D.R. 2004. On dense granular flows. The European Physical Journal E, **14**, 341-365, doi: 10.1140/epje/i2003-10153-0.

Ministry, C.R. 2008. Railway Industry Standard of the people's Republic of China TB/T2140-2008.

Muraro, S. & Jommi, C. 2019. Implication of end restraint in triaxial tests on the derivation of stress–dilatancy rule for soils having high compressibility. Canadian Geotechnical Journal, **56**, 840-851, doi: 10.1139/cgj-2018-0343.

Nie, Z., Liu, S., Hu, W. & Gong, J. 2020. Effect of local non-convexity on the critical shear strength of granular materials determined via the discrete element method. Particuology, doi: 10.1016/j.partic.2019.12.008.

Nie, Z., Zhu, Y., Zou, J., Gong, J. & Liu, S. 2019. DEM study of the microscopic characteristics and internal stability of binary mixtures. Powder Technology, **352**, 314-324, doi: 10.1016/j.powtec.2019.04.077.

O'Sullivan, C. & Cui, L. 2009. Micromechanics of granular material response during load reversals: Combined DEM and experimental study. Powder Technology, **193**, 289-302, doi: https://doi.org/10.1016/j.powtec.2009.03.003.

Paixão, A., Resende, R. & Fortunato, E. 2018. Photogrammetry for digital reconstruction of railway ballast particles – A cost-efficient method. Construction and Building Materials, **191**, 963-976, doi: 10.1016/j.conbuildmat.2018.10.048.

Potyondy, D.O. & Cundall, P.A. 2004. A bonded-particle model for rock. International Journal of Rock Mechanics and Mining Sciences, **41**, 1329-1364, doi: https://doi.org/10.1016/j.ijrmms.2004.09.011.

Qu, T., Feng, Y.T., Wang, Y. & Wang, M. 2019. Discrete element modelling of flexible membrane boundaries for triaxial tests. Computers and Geotechnics, **115**, doi: 10.1016/j.compgeo.2019.103154.

Rajan, B. & Singh, D. 2017. Understanding influence of crushers on shape characteristics of fine aggregates based on digital image and conventional techniques. Construction and Building Materials, **150**, 833-843, doi: 10.1016/j.conbuildmat.2017.06.058.

Rice, J. 1976. Localization of plastic deformation. Theoretical and applied mechanics.

Shire, T. & O'Sullivan, C. 2012. Micromechanical assessment of an internal stability criterion. Acta Geotechnica, **8**, 81-90, doi: 10.1007/s11440-012-0176-5.

Suhr, B., Skipper, W.A., Lewis, R. & Six, K. 2020. Shape analysis of railway ballast stones: curvature-based calculation of particle angularity. Scientific Reports, **10**, doi: 10.1038/s41598-020-62827-w.

Suiker Akke, S.J., Selig Ernest, T. & Frenkel, R. 2005. Static and Cyclic Triaxial Testing of Ballast and Subballast. Journal of Geotechnical and Geoenvironmental Engineering, **131**, 771-782, doi: 10.1061/(ASCE)1090-0241(2005)131:6(771).

Sun, Q., Indraratna, B. & Ngo, N.T. 2019. Effect of increase in load and frequency on the resilience of railway ballast. Geotechnique, **69**, 833-840, doi: 10.1680/jgeot.17.P.302.

Sun, Z., Espinoza, D.N. & Balhoff, M.T. 2018. Reservoir rock chemo-mechanical alteration quantified by triaxial tests and implications to fracture reactivation. International Journal of Rock Mechanics and Mining Sciences, **106**, 250-258, doi: 10.1016/j.ijrmms.2018.04.004.

Tong, L. & Wang, Y.H. 2014. DEM simulations of shear modulus and damping ratio of sand with emphasis on the effects of particle number, particle shape, and aging. Acta Geotechnica, **10**, 117-130, doi: 10.1007/s11440-014-0331-2.

Wadell, H. 1932. Volume, Shape, and Roundness of Rock Particles. The Journal of Geology, **40**, 443-451, doi: 10.1086/623964.

Wang, C., Deng, A. & Taheri, A. 2018. Three-dimensional discrete element modeling of direct shear test for granular rubber-sand. Computers and Geotechnics, **97**, 204-216, doi: 10.1016/j.compgeo.2018.01.014.

Wang, P. & Yin, Z.-Y. 2020. Micro-mechanical analysis of caisson foundation in sand using DEM. Ocean Engineering, **203**, doi: 10.1016/j.oceaneng.2020.107240.

Wang, X. 2020. Shape quantification, model reconstruction of geotechnical granular materials and application to discrete element modeling. Central South University.

Yang, J. & Dai, B.B. 2011. DEM analysis of soil fabric effects on behaviour of sand S. YIMSIRI and K. SOGA (2010).Géotechnique60, No. 6, 483–495. Geotechnique, **61**, 715-719, doi: 10.1680/geot.2011.61.8.715.

Yin, Z.-Y., Chang, C.S. & Hicher, P.-Y. 2010. Micromechanical modelling for effect of inherent anisotropy on cyclic behaviour of sand. International Journal of Solids and Structures, **47**, 1933-1951, doi: https://doi.org/10.1016/j.ijsolstr.2010.03.028.

Yin, Z.-Y., Hicher, P.-Y., Dano, C. & Jin, Y.-F. 2017. Modeling Mechanical Behavior of Very Coarse Granular Materials. **143**, C4016006, doi: doi:10.1061/(ASCE)EM.1943-7889.0001059.

Yin, Z.-Y., Wang, P. & Zhang, F. 2020. Effect of particle shape on the progressive failure of shield tunnel face in granular soils by coupled FDM-DEM method. Tunnelling and Underground Space Technology, **100**, doi: 10.1016/j.tust.2020.103394.

Zhu, H.-X. & Yin, Z.-Y. 2019. Grain Rotation-Based Analysis Method for Shear Band. Journal of Engineering Mechanics, **145**, doi: 10.1061/(asce)em.1943-7889.0001654.

Zhu, H.-X., Yin, Z.-Y. & Zhang, Q. 2020. A novel coupled FDM-DEM modelling method for flexible membrane boundary in laboratory tests. International Journal for Numerical and Analytical Methods in Geomechanics, **44**, 389-404, doi: 10.1002/nag.3019.